

Islands of oblate hyperdeformed and superdeformed superheavy nuclei with D_{3h} point group symmetry in competition with normal-deformed D_{3h} states: “Archipelago” of D_{3h} -symmetry islands

J. Yang ^{1,2}, J. Dudek ^{3,*}, I. Dedes ⁴, A. Baran ², D. Curien ³, A. Gaamouci ⁴,
A. Góźdź ², A. Pędrak ⁵, D. Rouvel ³ and H. L. Wang ¹

¹*School of Physics and Microelectronics, Zhengzhou University, Zhengzhou 450001, China*

²*Institute of Physics, Marie Curie-Skłodowska University, PL-20 031 Lublin, Poland*

³*Université de Strasbourg, CNRS, IPHC UMR 7178, F-67 000 Strasbourg, France*

⁴*Institute of Nuclear Physics Polish Academy of Sciences, PL-31 342 Kraków, Poland*

⁵*National Centre for Nuclear Research, Theoretical Physics Division, PL-02-093 Warsaw, Poland*



(Received 4 October 2022; revised 26 March 2023; accepted 7 April 2023; published 10 May 2023)

In two recent articles we have formulated nuclear mean-field theory predictions of existence of a new form of magic numbers, referred to as fourfold magic numbers. These predictions stipulate the presence of strong shell closures at the neutron numbers $N = 136$ (actinide region) and $N = 196$ (superheavy region) simultaneously at nonvanishing all four octupole deformations $\alpha_{3\mu=0,1,2,3} \neq 0$. In contrast to the traditional notion of magic numbers, the new notion refers to simultaneous nonspherical configurations ($\alpha_{3\mu} \neq 0, \alpha_{2\mu} = 0$). In this article we study the nuclear equilibrium deformations with $\alpha_{33} \neq 0$ combined with nonvanishing quadrupole deformation, $\alpha_{20} \neq 0$. One easily shows that such geometrical shapes have a threefold symmetry axis and are invariant under the symmetry operations of the D_{3h} point group. We employ a realistic phenomenological mean-field approach with the so-called universal deformed Woods-Saxon potential and its recently optimized parametrization based on actualized experimental data with the help of the *inverse problem theory* methods. The presence of parametric correlations among 4 of 12 parameters in total was detected and removed employing Monte Carlo approach leading to stabilization of the modeling predictions. Our calculations predict the presence of three nonoverlapping groups of nuclei with D_{3h} symmetry, referred to as islands on the nuclear (Z, N) plane (mass table). These islands lie in the rectangle $110 \leq Z \leq 138$ and $166 \leq N \leq 206$. The “repetitive” structures with the D_{3h} symmetry minima are grouped in three zones of oblate quadrupole deformation, approximately, at $\alpha_{20} \in [-0.10, -0.20]$ (oblate normal deformed), around $\alpha_{20} \approx -0.5$ (oblate superdeformed) and $\alpha_{20} \approx -0.85$ (oblate hyperdeformed). Importantly, the energies of those latter exotic deformation minima are predicted to be very close to the ground-state energies. We illustrate, compare, and discuss the evolution of the underlying shell structures. Nuclear surfaces parametrized as usual with the help of *real* deformation parameters, $\{\alpha_{\lambda\mu} = \alpha_{\lambda\mu}^*\}$, are invariant under \mathcal{O}_{xz} -plane reflection, the symmetry also referred to as y simplex (\mathcal{S}_y). For the shapes with odd-multipolarity ($\lambda \rightarrow \lambda_{\text{odd}} = 3, 5, 7, \dots$) it follows that $E(-\alpha_{\lambda_{\text{odd}},\mu}) = E(+\alpha_{\lambda_{\text{odd}},\mu})$. It turns out that the predicted equilibrium deformations generate symmetric double (or “twin”) minima separated by potential barriers, whose heights vary with the nucleon numbers, possibly inducing the presence of parity-doublets in the spectra. To facilitate possible experimental identification of such structures, we examine the appearance of such doublets solving the collective Schrödinger equation. Implied suggestions are illustrated and discussed.

DOI: [10.1103/PhysRevC.107.054304](https://doi.org/10.1103/PhysRevC.107.054304)

I. INTRODUCTION

Studying nuclear structure properties of exotic nuclei with possibly large numbers of either protons, Z , or neutrons, N , or both simultaneously and in particular the issue of their stability is one of the most actively followed research directions in contemporary subatomic physics. Whereas the experimental research is being performed in international laboratories using most performant instrumentation and focusing on the nuclear species which can be produced and detected contemporarily, theory applications address various methods

of modeling applied to broader areas of the nuclear mass table. Extending the theory investigations, sometimes far from the presently accessible nuclear mass areas, plays an important role stimulating the development of possibly even more performant instrumentations with the help of which, those today inaccessible zones, could hopefully be accessed in the future.

There is no place in this article to provide a review of this rich and fast growing subject but the interested reader might consult review articles, see, for instance, Refs. [1–6] and references therein. Instead, it will be instructive to overview selected aspects of this recent evolution, addressing superheavy nuclei—in particular in the areas of nuclear mass table of interest in this article.

*jerzy.dudek@iphc.cnrs.fr

One of the most important concepts, which allows constructing powerful approximate methods of modeling, is the empirical observation that nuclei governed by short-range strong interactions can be seen as compact objects with their volumes close to the sums of the volumes of the participating nucleons. Moreover, due to the short nuclear interaction range, the resulting nuclear density distributions decrease to zero exponentially at the borders of the corresponding systems. This latter general property justifies introduction of the notions of the nuclear surface and the corresponding shape, which both turn out to be the source of the precious and rich information for testing theory and experiment. This applies in particular to the issue of identification and examining the nuclear geometrical symmetries with the help of the point-group theory discussed in the recent Ref. [7].

The presence in nature of compact nuclear bodies with generally nonspherical shapes brings us to two directly related notions of capital importance for contemporary nuclear structure: The issue of the nuclear orientation with the implied phenomenon of collective rotations and angular momentum induced transitions and the issue of the shape oscillations and the phonon and multiphonon excitations. As one can immediately remark, the concept of nuclear shapes is extremely instructive and rich in various implications with *direct* relations to experiment. The corresponding conceptual evolution and underlying discoveries gave rise to the Nobel Prize to Bohr, Mottelson, and Rainwater in 1975, cf. also Ref. [8].

Several superheavy nuclei with $Z = 114$ – 118 were discovered and their identification confirmed through the hot fusion processes in the past twenty years or so, see for instance Refs. [9–12]. Today, the heaviest discovered superheavy elements include ${}_{114}^{288}\text{Fl}_{174}$, ${}_{116}^{292}\text{Lv}_{176}$, and ${}_{118}^{294}\text{Og}_{176}$, Ref. [13]. Attempts to produce or synthesize exotic elements with $Z \geq 120$ were discussed in Refs. [14–16]. In their recent review, Ref. [17], the authors discuss possible reactions producing superheavy nuclei. According to their estimates, nuclei in the $Z = 120$ and $N = 178$ – 182 zone are expected to have lifetimes of more than 90 ms.

The nuclear structure properties and global features of superheavy nuclei were studied in parallel in many theory projects over the past 70 years. One of the most important subjects to address was the stability island of superheavy nuclei.

Spherical shell closures with proton number $Z = 114$ and neutron number $N = 184$ were predicted for the first time in the superheavy region in Ref. [18], in 1966. These predictions were reproduced in the later studies in Refs. [19–21]; besides that, spherical magic numbers at $Z = 126$ and $N = 184$ were predicted in Ref. [19] within phenomenological mean field. Predictions employing microscopic techniques such as self-consistent Skyrme-Hartree-Fock-Bogolyubov approach within effective density-functional formalism can be found in Refs. [22,23].

The appearance of the spherical shell gaps at $Z = 114$, $N = 184$, alternatively $Z = 120$, $N = 172$ or $Z = 126$, $N = 184$, predicted employing spherical relativistic and nonrelativistic mean-field methods was discussed in Ref. [20]. The hypothetical magic numbers $Z = 120$ and $N = 184$ were also suggested in Refs. [21,24].

In this article we focus specifically on what we refer to as an archipelago of superheavy nuclei, which present various forms of the geometrical D_{3h} symmetry. The nuclei in question are contained in the mass range defined by the intervals $114 \leq Z \leq 132$ and $166 \leq N \leq 206$.

Our calculations were performed employing a realistic phenomenological mean-field Hamiltonian optimized using the *inverse problem theory* of applied mathematics, the approach employed in a recent study of Ref. [25]. The symmetry aspects are treated with the help of the group representation theory used to examine the impact of exotic nuclear point-group symmetries on the nuclear quantum observables. For this latter aspect the reader may consult Sec. IV of Ref. [7].

In what follows we present briefly the realization of the well-known macroscopic-microscopic method of Strutinsky, Refs. [26,27], in the version employed in this article. Presentation of the theoretical predictions accompanied by the discussion and comparisons will be given next. It turns out that predictions of the static nuclear equilibrium deformations may be misleading; we address the issue of the dynamical equilibrium deformations obtained by solving the collective model of Bohr as the next topic. Mathematical aspects related to the main focus of the article, D_{3h} molecular symmetry in subatomic physics, are presented in the Appendixes, where we address specificities of the spherical harmonics shape representation in terms of the *real* expansion coefficients $\alpha_{\lambda,\mu}$ (deformation parameters) and various implied symmetry aspects.

II. CALCULATION METHOD and MODELING DETAILS

The prediction of an existence of “an archipelago of islands” of superheavy nuclei manifesting D_{3h} molecular symmetry, which will be presented in this article, can be seen as an encouraging signal of new, challenging nuclear structure mechanisms. Related theoretical predictions address deformation properties of heavy and superheavy nuclei resulting from large-scale potential-energy calculations in multidimensional deformation spaces. The obtained information about shapes and shape competition can be linked with experiment for instance by examining specific rotational band properties as proposed in Ref. [7] or through selected electromagnetic transition properties. Indeed, the latter can be described with the help of multipole moments, $\hat{Q}_{\lambda,\mu}$, calculated from the deformations at the predicted potential-energy minima by deducing next the reduced transition probabilities and implied lifetimes directly comparable with experiment.

A. Phenomenological Woods-Saxon mean-field realization within macroscopic-microscopic method

In the following we present our results of the calculations of nuclear energies for superheavy nuclei in the mass range $114 \leq Z \leq 132$ and $166 \leq N \leq 206$. We calculate the nuclear energies using macroscopic-microscopic Strutinsky method, Refs. [26,27], with a realistic phenomenological mean-field Hamiltonian. We use a deformed Woods-Saxon potential in its “universal” parametrization, Refs. [28,29]. The

adopted realization follows closely the one employed and described in detail in Refs. [7,25].

According to Strutinsky approach the nuclear energy can be expressed as the sum of the so-called macroscopic and microscopic energy terms as follows:

$$E(Z, N) = E_{\text{mac}}(Z, N) + \delta E_{\text{mic}}^{(\pi)}(\{e_{\rho}^{(\pi)}\}) + \delta E_{\text{mic}}^{(v)}(\{e_{\rho}^{(v)}\}). \quad (1)$$

We use the macroscopic energy term in the FRLDM realization of Refs. [30], and parametrization from Ref. [31]. The so-called microscopic part of the energy expression, is given by the sum of two terms referred to as “shell” or “shell correction” and “pairing,” or “pairing correction” terms, respectively,

$$\delta E_{\text{mic}}^{(\pi, v)} = \delta E_{\text{shell}}^{(\pi, v)} + \delta E_{\text{pair}}^{(\pi, v)}, \quad (2)$$

according to standard notation.

The nuclear shapes are defined in terms of the spherical harmonic $\{Y_{\lambda\mu}\}$ expansion of the nuclear surface Σ :

$$\Sigma : R(\vartheta, \varphi; \alpha) = R_0 c(\alpha) \left[1 + \sum_{\lambda\mu} \alpha_{\lambda\mu}^* Y_{\lambda\mu}(\vartheta, \varphi) \right], \quad (3)$$

with deformation parameters,¹ in principle complex, represented by the spherical tensors $\{\alpha_{\lambda\mu}\} \leftrightarrow \alpha$ with non-negative integer indices λ and μ limited by $-\lambda \leq \mu \leq \lambda$. The radius parameter $R_0 = r_0 A^{1/3}$ (see below) whereas $c(\alpha)$ represents a deformation-dependent numerical factor assuring that the volume of the nucleus remains constant, independent of deformation.

There are several advantages of using spherical harmonics in the nuclear shape description. First, they form a complete set of orthogonal functions and thus can be employed as orthonormal basis. Second, they are the basis functions of the irreducible representations of the group SO(3), the group of rotations in three dimensions. The latter plays an important role, among others in describing the nuclear spatial orientations. Since the point-groups, and in particular the D_{3h} one, which are of central interest for the present project, are subgroups of SO(3), it follows that one can directly derive the links between the nuclear mean-field geometry and the nuclear quantum rotor properties related to nuclear orientation. The latter provide experimental identification criteria of the point-group symmetries. The reader interested in related mathematical aspects may consult Sec. IV B of Ref. [7], in particular, Eqs. (30) and (31) and the surrounding text. Further

¹In the following we need to express the energy dependence on nuclear deformations but the presence of the double index tensor notation $\alpha_{\lambda\mu}$ may occasionally lead to ambiguities. One type of the energy dependence used below, written as $E(\{\alpha_{\lambda\mu}\})$ or $E(\alpha)$, expresses a dependence on the ensemble of all the deformations. Another form, for instance, relations like $E(-\alpha_{33}) = E(\alpha_{33})$, emphasize a dependence on one deformation among others. Similarly expressions of the form $E(\alpha_{4\mu})$ or $E(\alpha_{\lambda\mu})$ emphasize dependencies on a single deformation.

specific mathematical properties related to nuclear geometry and exotic symmetries are summarized in Appendixes A and B.

The ensemble of single-nucleon energies, $\{e_{\rho}\}$, used in calculating the Strutinsky energies in Eq. (1), is obtained by solving numerically the Schrödinger equation with the Woods-Saxon mean-field Hamiltonian

$$\hat{H}_{WS} = \hat{T} + \hat{V}_{WS} + \hat{V}_{WS}^{so} + \hat{V}_{\text{Coulomb}}, \quad (4)$$

where \hat{T} denotes the nucleonic kinetic-energy operator and \hat{V}_{WS} is the central Woods-Saxon potential given by

$$\hat{V}_{WS}(\vec{r}, \alpha; V^c, r^c, a^c) = \frac{V^c}{1 + \exp[\text{dist}_{\Sigma}(\vec{r}, R^c; \alpha)/a^c]}, \quad (5)$$

whereas the spin-orbit potential is defined as usual with the help of the gradient of the Fermi-type functions by

$$\hat{V}_{WS}^{so}(\vec{r}, \hat{p}, \hat{s}, \alpha; \lambda^{so}, r^{so}, a^{so}) = \frac{2\hbar\lambda^{so}}{(2mc)^2} [(\vec{\nabla} V_{WS}^{so}) \wedge \hat{p}] \cdot \hat{s}, \quad (6)$$

where

$$V_{WS}^{so}(\vec{r}, \alpha; V^c, r^{so}, a^{so}) = \frac{V^c}{1 + \exp[\text{dist}_{\Sigma}(\vec{r}, R^{so}; \alpha)/a^{so}]}. \quad (7)$$

The nucleonic position is denoted by $\vec{r} \equiv \{x, y, z\}$, the symbols V^c, r^c, a^c , represent central potential depth, radius, and diffusivity parameters, respectively, whereas $\lambda^{so}, r^{so}, a^{so}$ stand for spin-orbit potential strength, radius, and diffusivity parameters, correspondingly. We have $R^c \equiv r^c A^{1/3}$ and $R^{so} \equiv r^{so} A^{1/3}$. The argument $\text{dist}_{\Sigma}(\vec{r})$ in the exponentials denotes the distance between the nucleon position point \vec{r} and the nuclear surface Σ .

With the two mean-field potentials, one for the protons and one for the neutrons, we have two Hamiltonians with two sets of six parameters each,

$$\{V^c, r^c, a^c; \lambda^{so}, r^{so}, a^{so}\}_{\pi, v}. \quad (8)$$

The resulting Schrödinger equations for both types of nucleons,

$$\hat{H}_{WS} \psi_{\rho} = e_{\rho} \psi_{\rho}, \quad (9)$$

are solved numerically employing standard harmonic-oscillator basis-expansion and diagonalization methods. To enable numerical applications of a basis composed in principle of infinite number of elements, a preselection of a finite number of them (basis cutoff) assuring an acceptable stability of the final diagonalization results is necessary. Obviously, the more the potential of interest deviates from the harmonic oscillator and the shapes of the nuclear surface from the spherical one, the higher the cutoff needed.

It turns out that increasing deformation parameters $\alpha_{\lambda\mu}$ leads directly to increasing the complexity in the spatial dependence of the potentials in Eqs. (5)–(7) and the need of larger and larger number of the harmonic-oscillator basis states to stabilize the final result: the single-nucleon energies. Since the richness of the nodal structure of the single nucleon wave function increases with increasing nucleon energy, these are the states with the highest-lying single-particle energies which are, on the average, the most sensitive with respect

to the basis cutoff. Combining the two properties, we optimized the deformed harmonic-oscillator (HO) basis adapting the basis cutoff in such a way that the highest single-particle energies at the extremities of the used deformation space (extremities of the tesseract) change with increase of the basis cutoff not stronger than at the third decimal place.

B. Selected symmetry properties: Nuclear surfaces and mean-field Hamiltonians

In the present project we employ multidimensional deformation spaces, in which the quadrupole deformation subspace $\{\alpha_{20}, \alpha_{22}\}$ is combined with the octupole deformation subspace $\{\alpha_{30}, \alpha_{31}, \alpha_{32}, \alpha_{33}\}$, supplemented with the hexadecapole one composed of α_{40}, α_{42} , and α_{44} . Within our deformation space the D_{3h} -symmetric nuclear surfaces involve either deformation α_{33} pure, or combined with axial quadrupole, α_{20} and/or axial hexadecapole α_{40} deformations. Higher-order- λ spherical harmonics with $\mu = \pm 3$ may also generate the D_{3h} symmetry. We verified that they do not have any significant impact in the present context and therefore were not included in the calculations.

Under certain conditions, cf. Appendix A, the nuclear surfaces defined by the deformation parameters, $\alpha_{\lambda\mu}$, and its opposite, $-\alpha_{\lambda\mu}$, represent exactly the same geometrical figures except for the orientation with respect to the original reference frame. As a consequence, for any single deformation with this property, the corresponding nuclear mean-field Hamiltonians satisfy the symmetry

$$\hat{\mathcal{H}}_{\text{mf}}(-\alpha_{\lambda\mu}) = \hat{\mathcal{H}}_{\text{mf}}(+\alpha_{\lambda\mu}) \quad (10)$$

and it follows that the same is valid for the resulting nuclear energies

$$E(-\alpha_{\lambda\mu}) = E(\alpha_{\lambda\mu}). \quad (11)$$

Therefore one can limit numerical calculations, e.g., to a positive, $\alpha_{\lambda\mu} > 0$ semi-axis of the related deformation, thus gaining a factor of two in terms of the computing time.

The symmetry relations in Eqs. (10) and (11), apply in particular to all the four octupole deformations $\alpha_{3;\mu=0,1,2,3}$ discussed in this article so that

$$E(-\alpha_{3\mu}) = E(\alpha_{3\mu}), \quad \mu = 0, 1, 2, 3, \quad (12)$$

in particular for the nuclei for which we find the equilibrium deformations with the shapes invariant under the D_{3h} symmetry point group. In the simplest variant, i.e., all deformations vanishing except for $\alpha_{33} \neq 0$, and recalling that $\alpha_{33} = -\alpha_{3-3}$, cf. Appendix A, the corresponding D_{3h} symmetric surface takes the form

$$R(\theta, \varphi; \alpha_{33}) \propto \{1 + \alpha_{33}[Y_{33}(\vartheta, \varphi) - Y_{3-3}(\vartheta, \varphi)]\}. \quad (13)$$

Results of our macroscopic-microscopic calculations suggest that molecular point-group symmetry D_{3h} appears as the shape-symmetry of many heavy and superheavy nuclei. Anticipating the detailed presentation of the calculation results later in the article it will be instructive to illustrate at this point some of the corresponding elementary geometrical features, cf. Fig. 1.

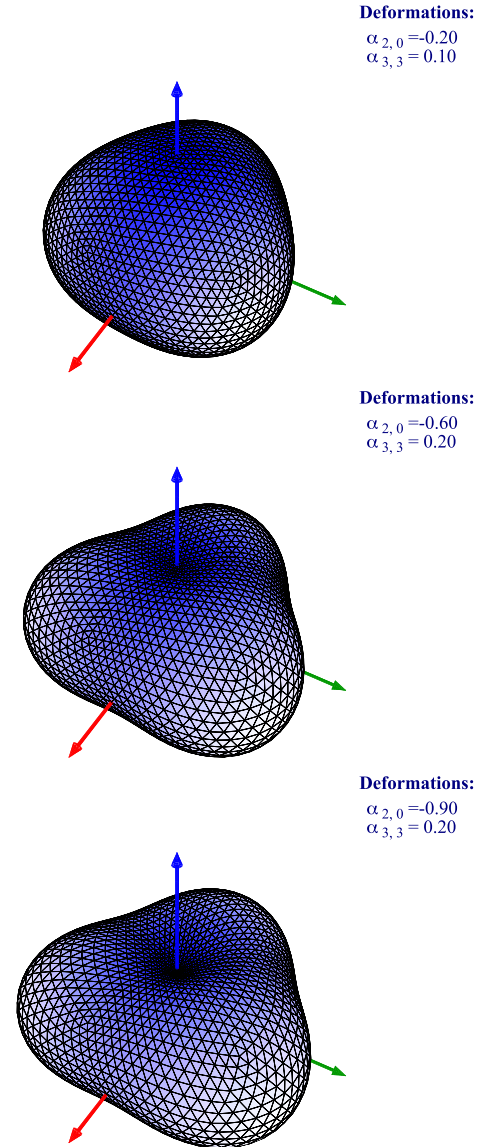


FIG. 1. Illustration of D_{3h} symmetric nuclear surfaces corresponding to local minima of the potential energies discussed in this article. Red, green, and blue arrows represent O_x , O_y , and O_z axes, respectively. (upper panel) Example of a shape referred to as “normal deformed,” here with $\alpha_{20} = -0.20$ and $\alpha_{33} = 0.10$. (middle panel) Strong, oblate deformation referred to as superoblate with $\alpha_{20} = -0.60$ and $\alpha_{33} = 0.20$ and (bottom panel) using similar terminology, hyperoblate one, with $\alpha_{20} = -0.90$ and $\alpha_{33} = 0.20$. The vertical axis coincides with the highest rank threefold symmetry axis, \mathcal{C}_3 operation with the rotation angle $2\pi/3$ (or 120°).

From the experimental symmetry-identification view point, the studied D_{3h} configurations might influence the quantum mechanism engaged in experiment quite differently. For instance some collective vibrations may signal their presence via inherent parity doublet excitations, cf. Sec. IV. The strongly oblate (super- or hyperdeformed) shapes are expected to have relatively low decay barrier; we avoid using at this point the term “fission barrier” because with the shapes predicted (see illustrations in Fig. 1, especially the middle and

bottom panels) the expected decay mode via barrier penetration will be that of a tripartition. Consequently, *observation of three fragments of comparable masses* could serve as a precious experimental identification help in the present project.

III. MULTIDIMENSIONAL POTENTIAL ENERGIES: RESULTS AND DISCUSSION

Let us begin by presenting typical results obtained using our realization of the macroscopic-microscopic method with the help of selected representative examples of nuclear potential-energy surfaces.

A. Main characteristics of two-dimensional energy projections in the deformation space employed

In the preceding sections we introduced the nuclear deformations with the help of the multipole expansion and the basis of spherical harmonics, $\{Y_{\lambda\mu}\}$, together with the associated deformation parameters $\{\alpha_{\lambda\mu}\}$. We need to provide an optimal selection of the retained multipolarities by beginning with the lowest- λ terms and adding the higher ones within the cutoff imposed by the computing systems at our disposal. Such a step by step approach is supported also by arguments based on the liquid drop model, Ref. [31] and references therein. Indeed, it turns out that the liquid-drop surface-energy increases significantly faster for a higher λ than for a smaller one. In other words: On average, $\alpha_{\lambda\mu}$ with higher order λ , produce much faster growing contributions of the macroscopic energy as compared with lower λ contributions and can often be neglected when addressing the lowest energies. Some practical criteria in decision taking within a semiquantitative trial and error multipolarity optimization search can be schematized as follows.

To begin we selected the following reference deformation sets: $\{\alpha^{\text{ref}}\}_{\mu} = \{\alpha_{20}, \alpha_{22}, \alpha_{3\mu=0,1,2,3}, \alpha_{40}\}$, one set per each octupole deformation $\alpha_{3\mu}$, and calculated the corresponding energy landscapes, which generally contain competing local minima. We verified that in the discussed (Z, N) mass table area, the nonaxial quadrupole deformation α_{22} does not lead to lowering the energies of the minima of principal interest, whereas $\alpha_{33} \neq 0$ (in contrast to α_{30}, α_{31} and α_{32}) generates low-lying minima.

Next we examined possible impacts of alternative deformation(s). Profiting from the fact that α_{22} was shown to play only a secondary role we replaced it and considered the sets of the structure $\{\alpha_{20}, \alpha_{33}, \alpha_{40}, \alpha_{\lambda',\mu'}\}$ with $\alpha_{\lambda',\mu'}$ chosen as $\alpha_{42}, \alpha_{44}, \alpha_{50}$, or α_{60} and tested the impacts of the newly added components on the local minima and the heights or widths of the potential barriers separating the competing minima. After comparisons, we retained $\{\alpha_{20}, \alpha_{22}, \alpha_{33}, \alpha_{40}\}$ selection for all the energy minimizations illustrated in this article.

We begin with the results for three representative nuclei: ${}^{302}_{118}\text{Og}_{184}$, ${}^{292}_{124}\text{Ubq}_{168}$, and ${}^{318}_{130}\text{Utn}_{188}$, Fig. 2, each one illustrating its group of neighbors forming the three “islands of the archipelago,” with the following properties:

- (i) case ${}^{302}_{118}\text{Og}_{184}$: D_{3h} -symmetric, oblate, normal deformed nuclei, $\alpha_{33} \neq 0$ and $\alpha_{20} \in [-0.15, -0.20]$;

- (ii) case ${}^{292}_{124}\text{Ubq}_{168}$: D_{3h} -symmetric, oblate, superdeformed nuclei, $\alpha_{33} \neq 0$ and $\alpha_{20} \in [-0.50, -0.60]$;
- (iii) case ${}^{318}_{130}\text{Utn}_{188}$: D_{3h} -symmetric, oblate, hyperdeformed nuclei, $\alpha_{33} \neq 0$ and $\alpha_{20} \in [-0.80, -0.90]$.

Our approach leads to four-dimensional (4-D) potential-energy landscapes. To present them as contour plots in the different figures of this article, we have minimized the energy according to the other deformation parameters. For example, to determine Fig. 2, we have minimized the energy according to α_{33} and α_{40} while keeping α_{20} and α_{22} (the axes of the figure) constant.

At this point, commenting about graphical conventions followed in this article will be in place. First, we wish to avoid causing false interpretation of, e.g., structures of the barriers, energy valleys, etc., possibly caused by the fact that the units on the horizontal and vertical axes are different, e.g., set arbitrarily by the plotting system. Therefore we assure that the step sizes on the x and y axes representing dimensionless variables $\alpha_{\lambda\mu}$ and $\alpha_{\lambda'\mu'}$ are strictly the same. Consequently, the landscape characteristics such as for instance widths of the potential barriers separating the minima remain comparable from one plot to another. In other words, they appear without distortions introduced by random choices of the scaling factors of the axes—possibly reflecting the author sense of aesthetic.

Another remark is related specifically to the potential-energy landscapes in Figs. 2 and 3: Given strong differences in the quadrupole deformation ranges for the upper, middle, and bottom panels, 1.2, 1.5, and 1.8, respectively, the sizes of the y axes of the plots were adjusted appropriately to obey the convention of equal unit lengths on both axes.

The projections on the quadrupole deformation plane $(\alpha_{20}, \alpha_{22})$ are equivalent, in terms of the so-called Bohr (β, γ) representation to $\beta \geq 0$ and $\gamma \in [0^\circ, 360^\circ]$, Fig. 2. We do not employ here the limitation sometimes referred to as “camembert sectors,” with $\gamma \in [0^\circ, 60^\circ]$ diagrams frequently seen in the literature. This is because we use simultaneously quadrupole and other deformations for which case such a limitation would have been misleading or even wrong.

Nuclear potential energies illustrated in Fig. 2 are projected on the $(\alpha_{20}, \alpha_{22})$ quadrupole deformation plane, after minimization over α_{33} and α_{40} —for ${}^{302}_{118}\text{Og}_{184}$, ${}^{292}_{124}\text{Ubq}_{168}$, and ${}^{318}_{130}\text{Utn}_{188}$. The three specific nuclei were selected for the present comparison for two reasons. First, all presented cases will be shown to manifest the D_{3h} symmetry in the ground or lowest-excited states. Second, each of them can be seen as representing an ensemble of several surrounding nuclei combining a certain common feature: An increasing degree of flattening in terms of the quadrupole deformation α_{20} combined with α_{33} deformation.

From Fig. 2 we can verify directly that the lowest-lying minima correspond to vanishing quadrupole triaxiality, $\alpha_{22} = 0$, combined with $\alpha_{20} \approx -0.15$ (upper panel), representing ${}^{302}\text{Og}$ and its several neighbors in the mass table, as compared with $\alpha_{20} \approx -0.50$ (middle panel), ${}^{292}\text{Ubq}$ and its neighbors, and finally $\alpha_{20} \approx -0.90$ (bottom panel), representative for ${}^{318}\text{Utn}$ and its neighbors. The α_{22} vs α_{20} projection does not allow us to deduce directly whether the minima correspond

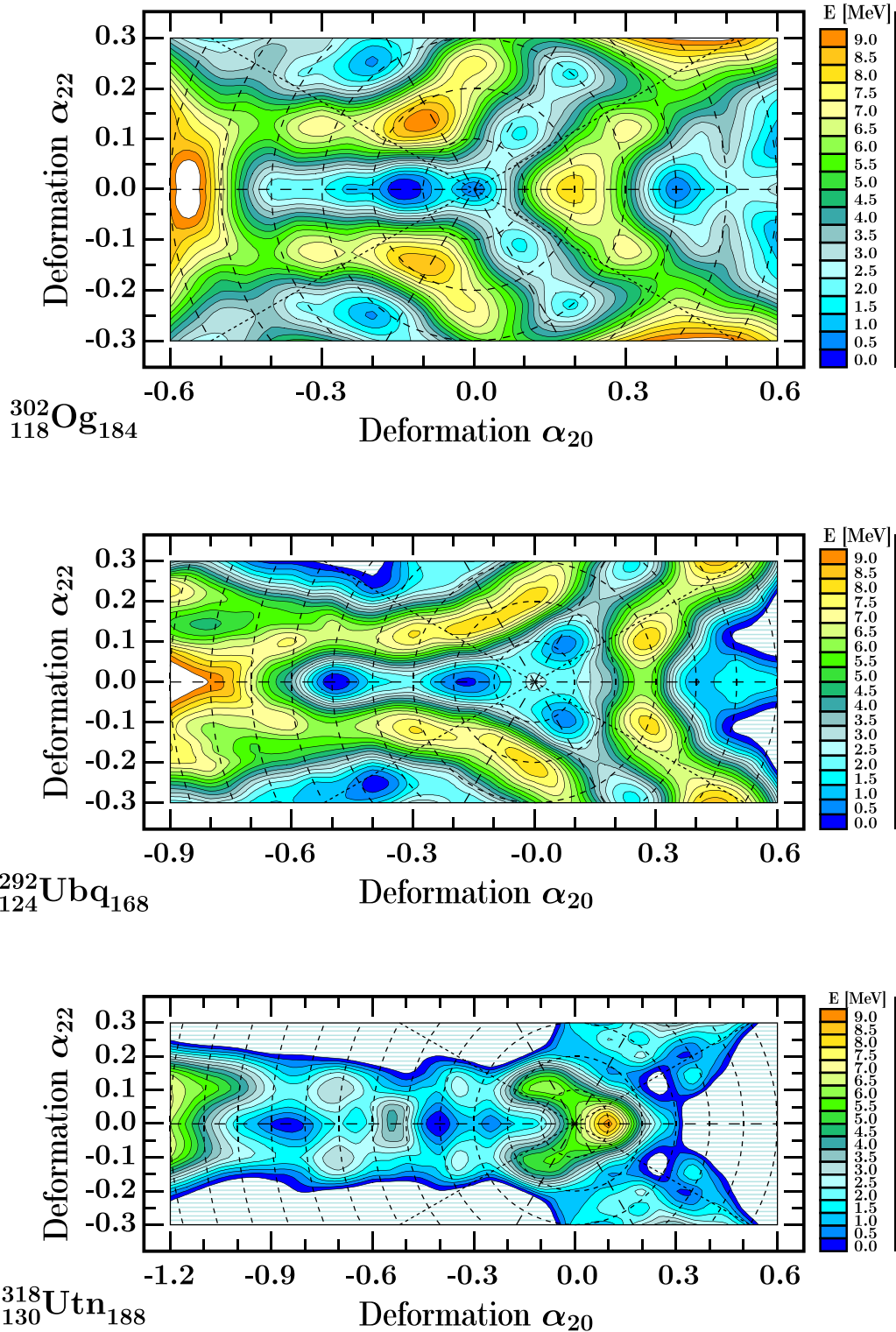


FIG. 2. Two-dimensional projections on the $(\alpha_{20}, \alpha_{22})$ plane of the nuclear potential energies calculated originally in the four-dimensional space of variables $\{\alpha_{20}, \alpha_{22}, \alpha_{33}, \alpha_{40}\}$. Each point represents the result of minimization over α_{33} and α_{40} . Whereas the diagrams show rather rich shape coexistence, which in itself is worth interest, here we would like to focus on the $\alpha_{22} = 0$ lowest energy minima: For ^{302}Og at $\alpha_{20} \approx -0.15$, for ^{292}Ubq at $\alpha_{20} \approx -0.50$ and for ^{318}Utn at $\alpha_{20} \approx -0.85$, corresponding to configurations referred to as oblate *normal*-, *super*-, and *hyperdeformed*, respectively. All three mentioned minima will be shown in the following figure to correspond to significant $\alpha_{33} \neq 0$, and thus to D_{3h} -symmetry configurations. The quadrupole nonaxial symmetry minima at $\alpha_{22} \neq 0$, slightly higher in energy, can be considered of general nuclear structure interest, however, they are not relevant for our discussion of the D_{3h} symmetry aspects.

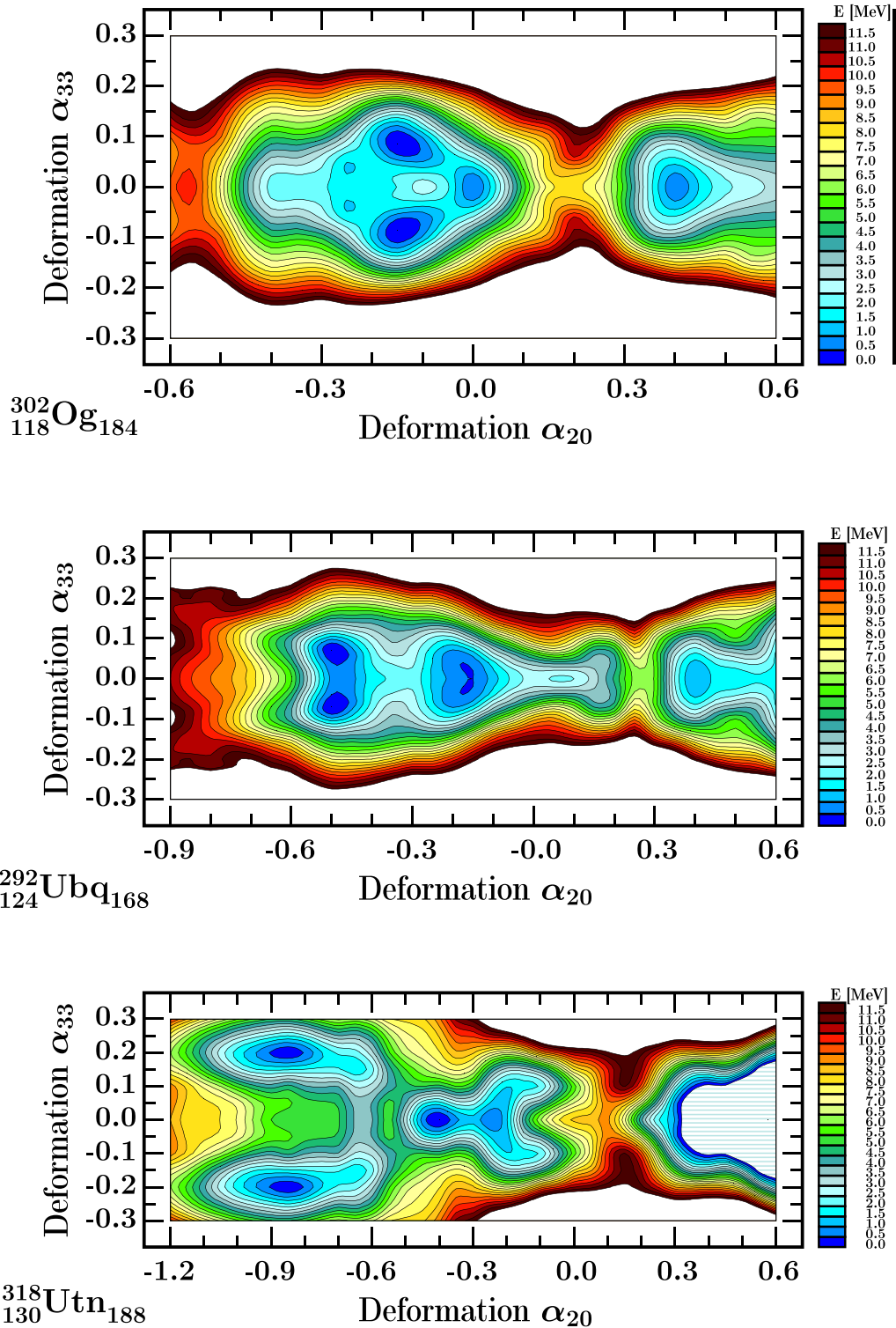


FIG. 3. Illustration analogous to the one in Fig. 2 but with modified role of deformation parameters: Projection on the two-dimensional plane of variables α_{33} vs α_{20} after minimizing over the remaining two variables, α_{22} and α_{40} . Let us emphasize the presence of the D_{3h} -symmetry minima with $\alpha_{33} \approx -0.10$ superposed with oblate normal deformed component $\alpha_{20} \approx -0.15$ in ^{302}Og (upper panel) and superdeformed one with $\alpha_{20} \approx -0.50$ in ^{292}Ubq (middle panel), respectively, compared with the ^{318}Utn case (bottom panel), with $\alpha_{33} \approx -0.20$ combined with $\alpha_{20} \approx -0.90$, thus referred to as hyperdeformed. Everyone among these three examples should be considered as representative for an ensemble of several nuclei in their respective neighborhoods in the mass table.

to the nonvanishing α_{33} shape component. Therefore this information is provided in Fig. 3, which shows double (twin) minima satisfying the condition $E(-\alpha_{33}) = E(+\alpha_{33})$, here combined with decreasing $\alpha_{20} \approx -0.15, -0.50$ and -0.90 . The figure shows total-energy projections for the same nuclei but with the projection $(\alpha_{20}, \alpha_{22})$ replaced by the projection $(\alpha_{20}, \alpha_{33})$.

We conclude that by allowing for the minimization over α_{33} and α_{40} within each $(\alpha_{20}, \alpha_{22})$ projection, the double minima gain approximately as follows: ^{302}Og , about 2 MeV at $\alpha_{20} = -0.15$; ^{292}Ubq , about 1 MeV at $\alpha_{20} = -0.50$ and ^{318}Utn , about 5.5 MeV at $\alpha_{20} = -0.90$. Since each of the three nuclei is representative for dozens of similar cases in the neighborhoods, we conclude that the new symmetry can be sought experimentally in some dozens of nuclei in the corresponding zones, see also comparisons in Figs. 7–10 in the next sections.

Our calculations suggest yet another mechanism representing the properties of coupling or decoupling between various multipolarities. To see explicitly what is meant, we compare the next selection of two-dimensional (2-D) illustrations, projections on the $(\alpha_{33}, \alpha_{22})$ -plane presented in Fig. 4. These results indicate that the D_{3h} -symmetry structures do not couple at all with the quadrupole-triaxial ones. Information of this type is very useful, when investigating a possible perturbation of the D_{3h} symmetry by other geometrical forms: In the present case we are allowed to ignore coupling with α_{22} at least to an approximation.

Yet another independence helping to simplify the interpretation of the shape correlations (or, following an alternative language, the “multipolarity independence”) is shown in Fig. 5 suggesting that the D_{3h} geometry does not couple with the other octupole degrees of freedom, i.e., neither α_{30} , nor α_{31} , nor α_{32} . Indeed, this can be immediately seen from the projections $(\alpha_{30}, \alpha_{20})$ vs $(\alpha_{31}, \alpha_{20})$ vs $(\alpha_{32}, \alpha_{20})$ shown in the upper, middle, and bottom panels, respectively. This type of information can be interpreted as “good news” for programming experiments, which aim not only at finding the signals of the corresponding superheavy nuclei but also identification of the D_{3h} symmetry in these nuclei via rotational band properties discussed in detail in Ref. [7].

B. From magic shell gaps in single-particle spectra to shell energies

Discussions of an occurrence and competition between nuclear potential-energy minima are often accompanied in the literature by illustrations presenting openings in the single-particle energy spectra (shell-gaps). The presence of such gaps and of the shell-energy minima goes hand-in-hand according to the theorem by Strutinsky—the single-particle energy diagrams having advantage of a relative compactness and simplicity.

Figure 6 illustrates the single-nucleon energy levels corresponding to varying octupole deformation α_{33} and thus suggesting the presence of the shell effects, which are expected to generate the nuclear energy minima carrying the D_{3h} -symmetric structures. The diagrams show the presence of some gap openings in the vicinity of $N = 196$ and 202 – 206

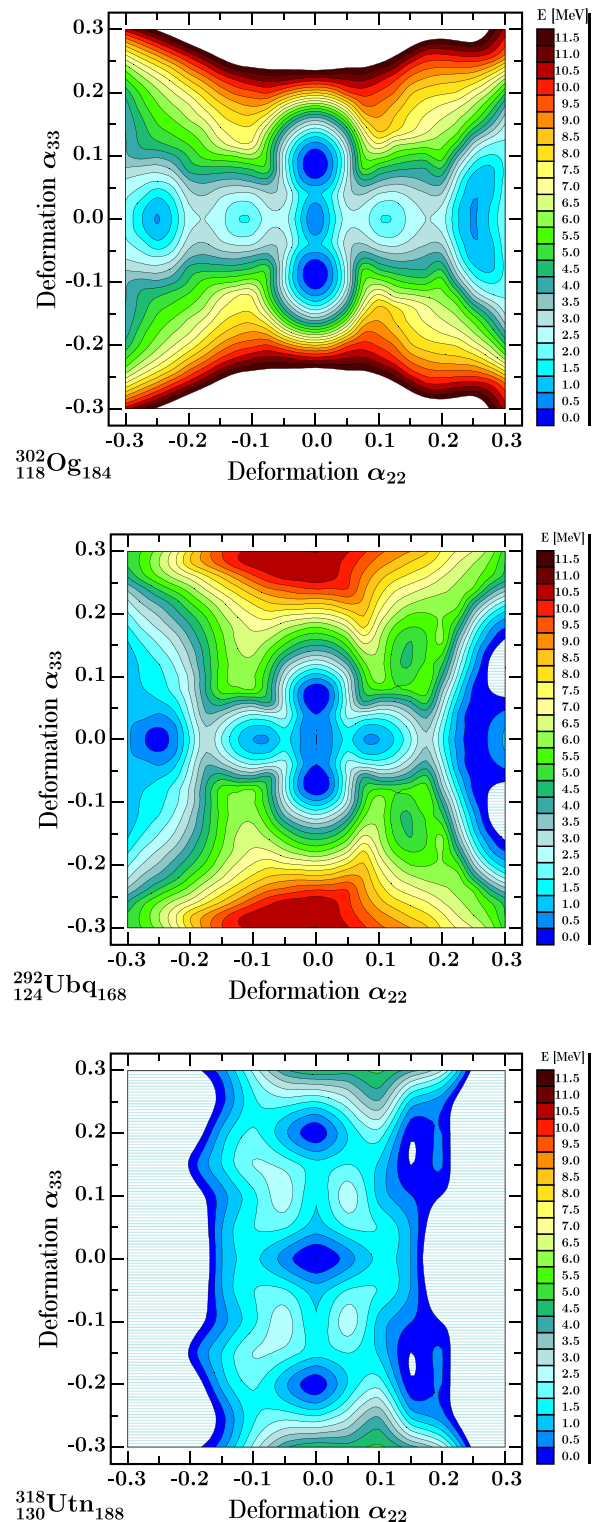


FIG. 4. Illustration of yet another type of total-energy projection, $(\alpha_{33}, \alpha_{22})$, manifesting what we call a decoupling of the quadrupole triaxiality α_{22} deformation, from the D_{3h} -symmetry-imposing α_{33} deformation. Observe that the D_{3h} minima at $\alpha_{33} \neq 0$ are well localized at vanishing α_{22} (null quadrupole triaxiality).

or Z around 118–122 suggesting that the corresponding nuclei are expected to play a leading role—but the diagrams of this kind cannot provide more quantitative suggestions.

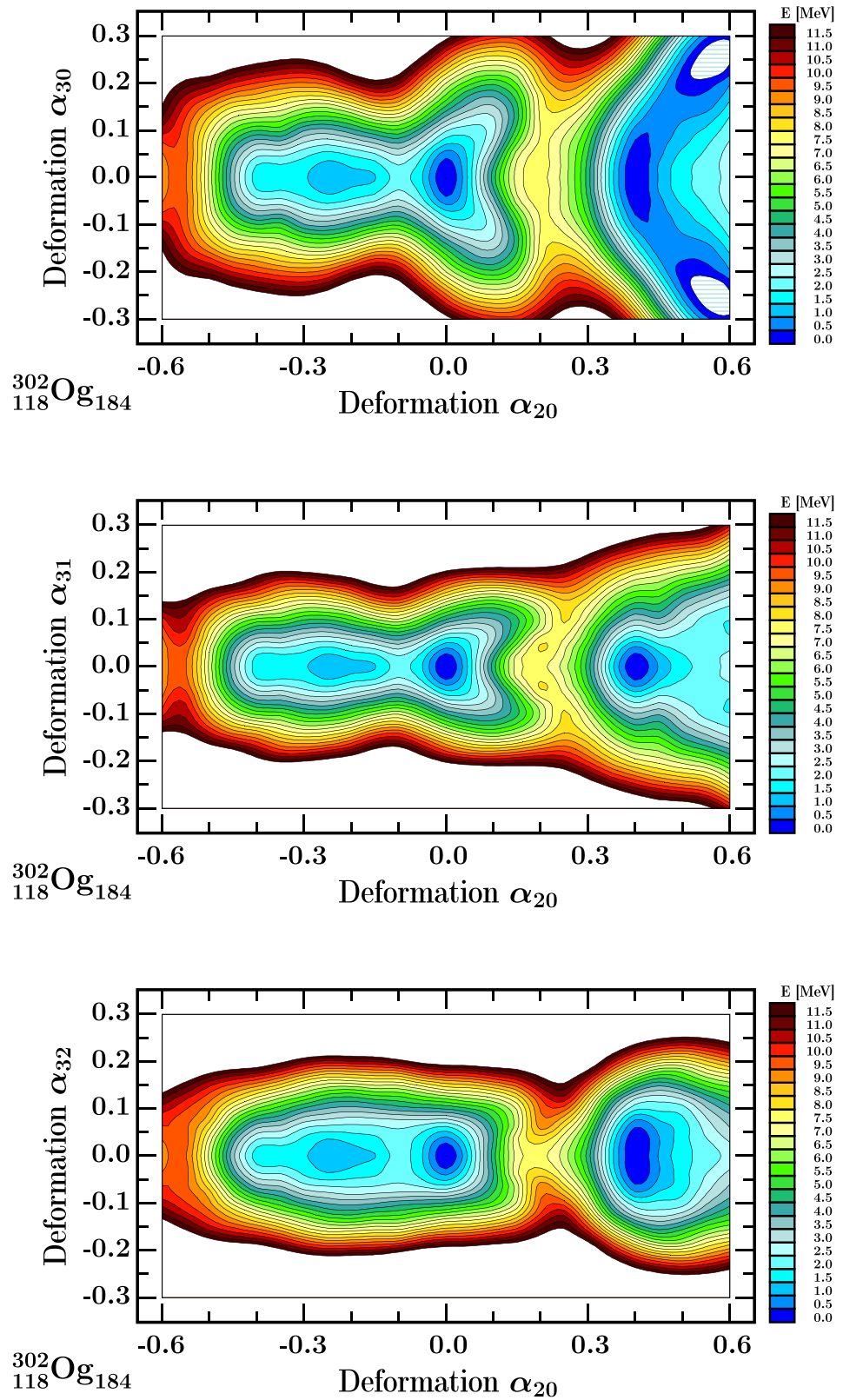


FIG. 5. Diagrams illustrating the properties of coexistence (or rather lack of coexistence) between the D_{3h} -symmetry octupole forms $\alpha_{33} \neq 0$ and the remaining octupole deformations. Indeed, whereas ^{302}Og manifests well pronounced $\alpha_{33} \neq 0$ minima, cf. Fig. 3, none of the competing octupole deformations leads to static minima as seen from the three projections. Results seen are characteristic for many nuclei in the mass range discussed in this article.

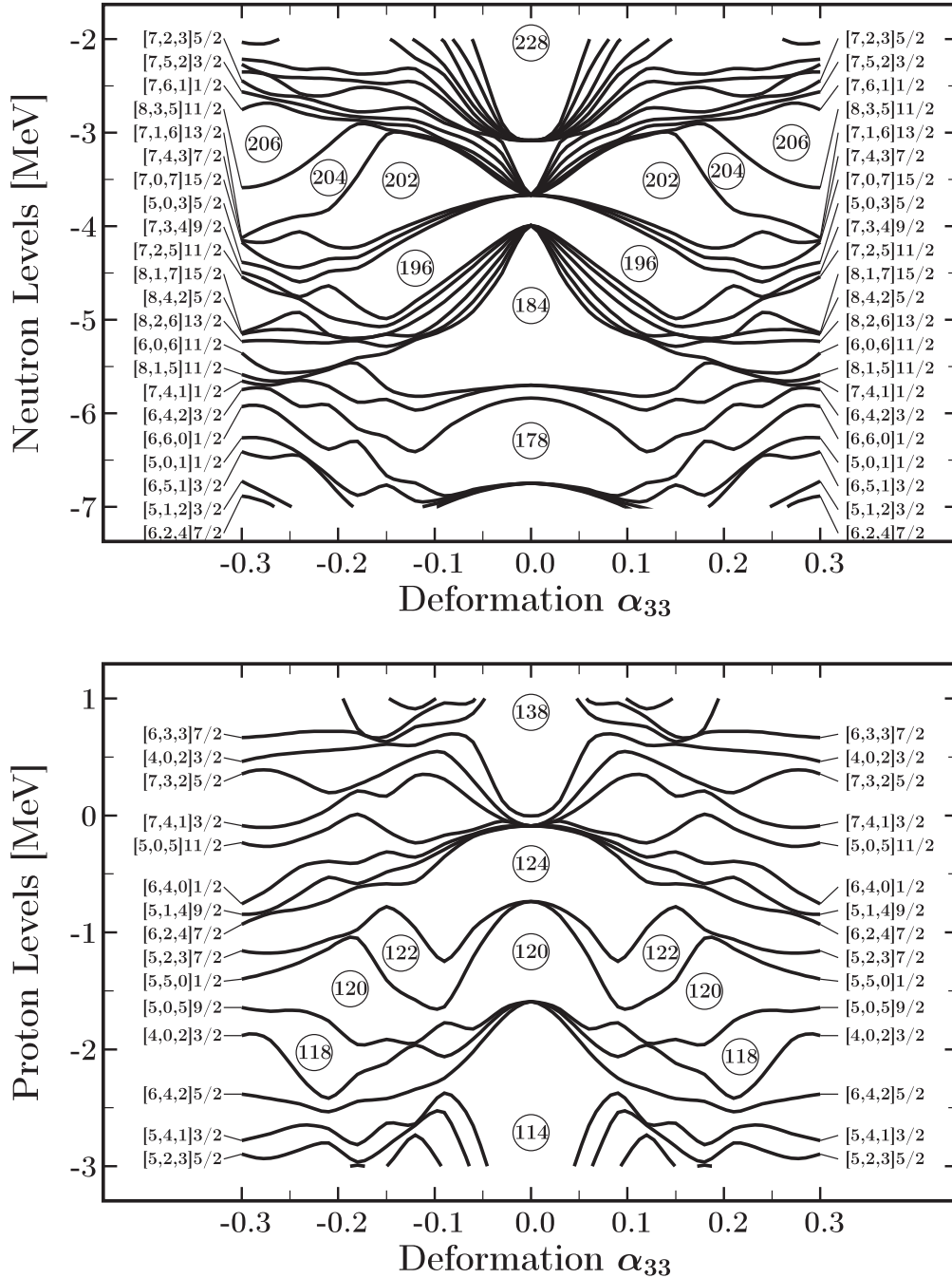


FIG. 6. (upper panel) Single-neutron energy levels obtained using the universal mean-field Hamiltonian discussed in this article—as functions of the D_{3h} -symmetry generating deformation α_{33} at $\alpha_{20} = 0$, for details see the text. Whereas certain gaps open with increasing α_{33} , cf. neutron number $N = 196$ as well as at $N = 202$, 204 , and 206 —at $N = 178$ and 184 they manifest a certain independence of α_{33} (remain approximately constant). (bottom panel) Similar to the preceding one but for the protons. Characteristic sequence of the octupole shell-openings at $Z = 118$, 120 , and 122 and the flatness at $Z = 124$ deserve noticing.

In these diagrams we fix the quadrupole deformation equal to zero, and this despite the fact that nuclei discussed in this project have by definition at least two significant nonvanishing deformations: α_{33} responsible for D_{3h} symmetry and quadrupole-oblate, either hyper-deformed, or superdeformed or normal-deformed. The idea behind fixing $\alpha_{20} = 0$ is a “pedagogical” one, since as it turns out, the pure octupole

deformations present the underlying characteristic octupole shell-gap structures in the clearest fashion—the gaps are the largest. In this way one should be able to reveal the leading shell effects in the simplest fashion and present the analogous octupole tendencies superposed with the quadrupole distortions using the *shell energies* rather than *single-particle energies*.

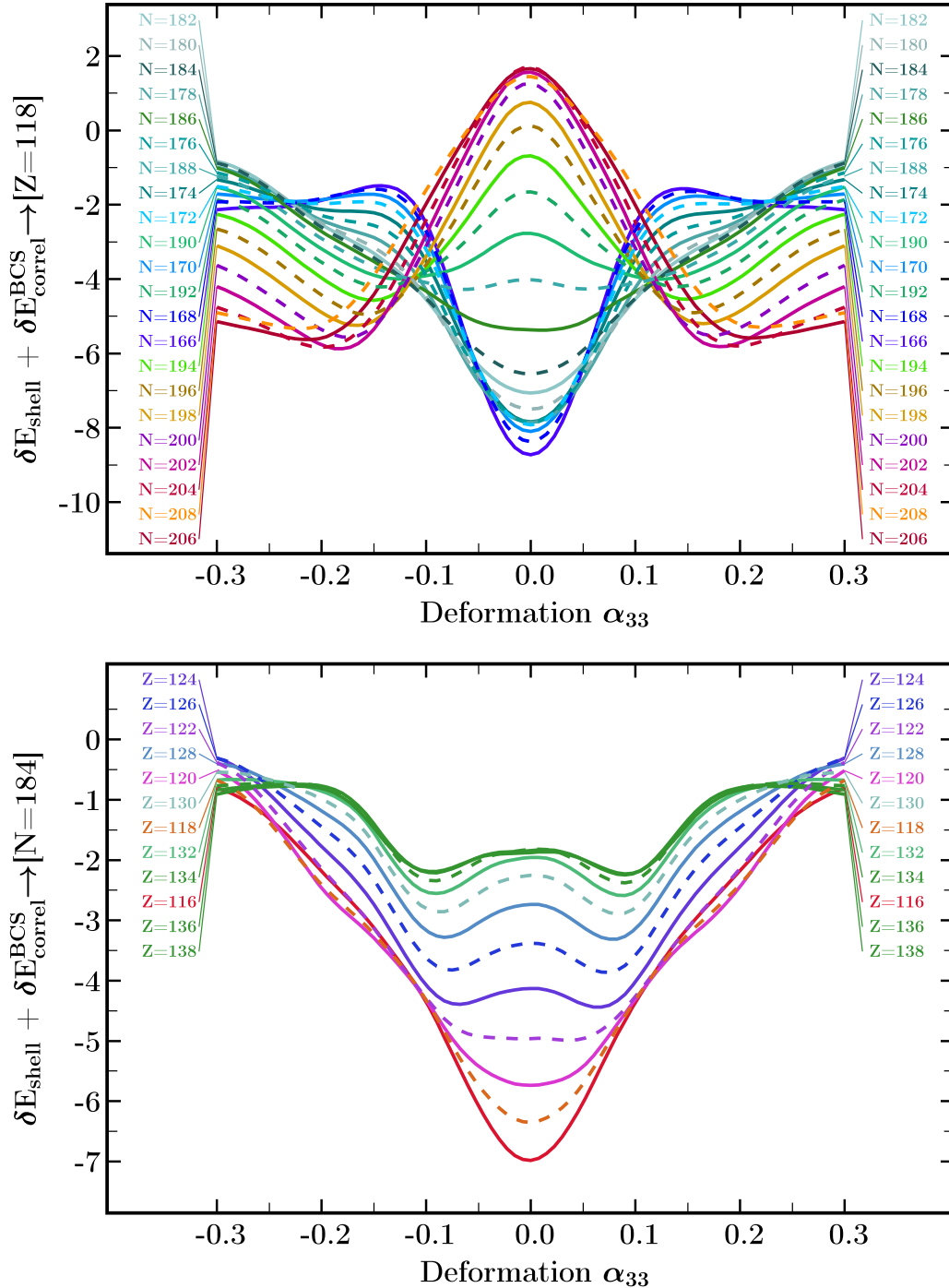


FIG. 7. (upper panel) Neutron shell energies defined as sums of the Strutinsky and pairing correction energies, for the isotopes labeled with the neutron numbers at fixed proton number $Z = 118$. Observe the strongest D_{3h} -symmetry driving effects at $N \approx 202$ compared with the opposite effect at $N \approx 168$. (bottom panel) Analogous illustration for the protons at fixed neutron number $N = 184$ selected as a representative case.

It will be instructive to compare directly the size of the shell effects, specifically for the protons and the neutrons in the nuclei corresponding to the cited big-gap generating particle numbers and their neighbors. This will allow us to learn reading the single-particle energy diagrams like those in Fig. 6 by providing direct quantitative

comparisons with the nuclear energies. Indeed, Fig. 7, upper diagram, shows the sums of the neutron shell and pairing energy contributions to the macroscopic energy in the framework of the macroscopic-microscopic approach, whereas the lower one illustrates the same for the protons.

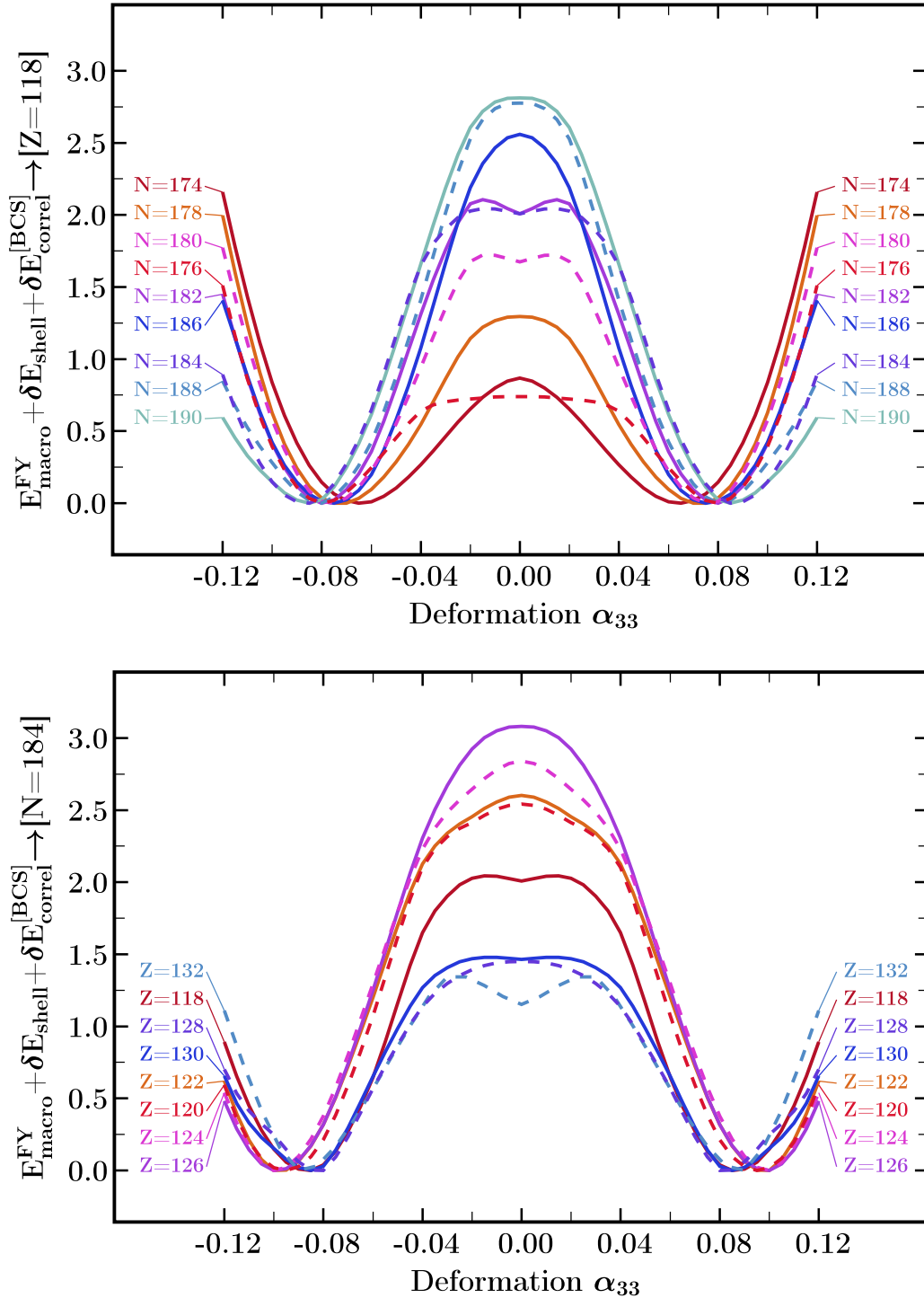


FIG. 8. (upper panel) Nuclear potential energy cross sections for fixed $Z_0 = 118$ and the neutron number varying in the interval $174 \leq N \leq 190$ as functions of α_{33} deformation. The energies are normalized to zero at the minimum. All the nuclei presented have the quadrupole α_{20} components at the equilibrium close to $\alpha_{20} \approx -0.20$ (“normal oblate”). Observe that in the case of $N = 190$ the nucleus gains nearly 3 MeV by becoming D_{3h} symmetric. The corresponding weakest variation (at $N = 174$) is nearly three times smaller. (bottom panel) Analogous to the preceding one but for varying proton number at fixed central neutron number $N = 184$. Observe again an energy gain of about 3 MeV, when allowing for the α_{33} variation in the case of the proton number $Z = 126$.

More precisely, the upper diagram in Fig. 7 shows the nuclear shell-energies for isotopes of the $Z = 118$ (Og) nucleus covering the neutron number range $N \in [166, 208]$. The strongest variation (lowering) of the shell energies with

α_{33} growing from 0 to about 0.2, corresponds indeed to the neutron numbers in the subinterval $[196, 206]$ as seen by reading the occupation numbers in Fig. 6, upper diagram. These neutron shell effects can be considered “huge”

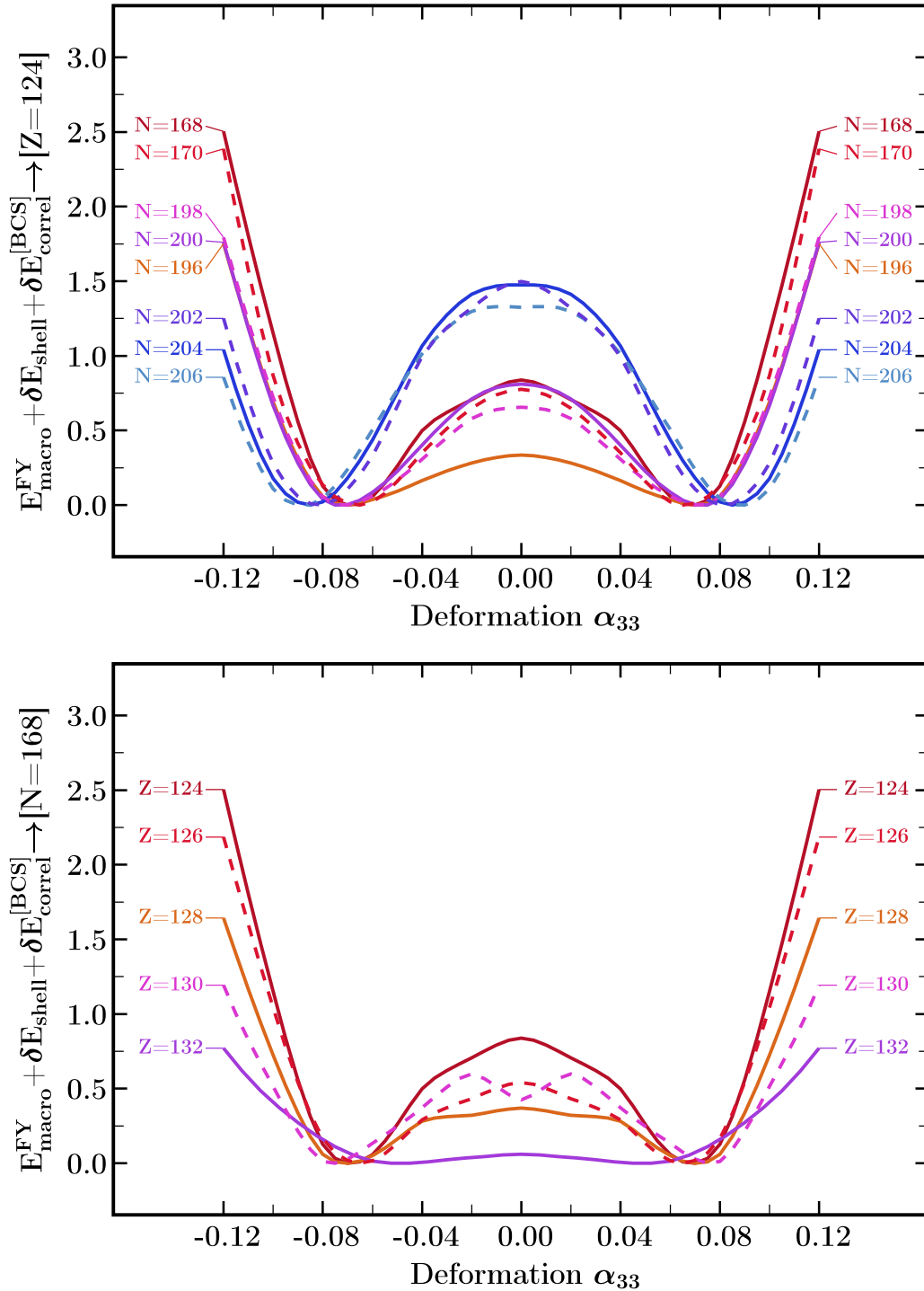


FIG. 9. Results similar to those in the preceding figure but for the D_{3h} -symmetric configurations with oblate quadrupole components $\alpha_{20} \approx -.50$ (“superdeformed oblate”). (upper panel) Total energies for the varying neutron numbers as displayed, for the central nucleus with proton number $Z_0 = 124$. We remark that the energy gain due to increasing α_{33} deformation is markedly less significant and amounts to about 1.5 MeV at, and close to the central neutron number $N_0 = 204$. (bottom panel) Similar to the above but for varying proton number at the fixed central neutron number $N_0 = 168$.

given the fact that the strongest variation, at $N = 202$, corresponds to over 7 MeV energy gain, thus a 7 MeV decrease, with growing α_{33} . Conversely, a comparable increase in the shell energy is observed for neutron numbers in the vicinity of $N = 172$.

C. Archipelago of D_{3h} -symmetric superheavy nuclei: An overview of D_{3h} -symmetry islands

In preceding sections we have pointed out to the presence of three groups of D_{3h} -symmetric nuclei centered at

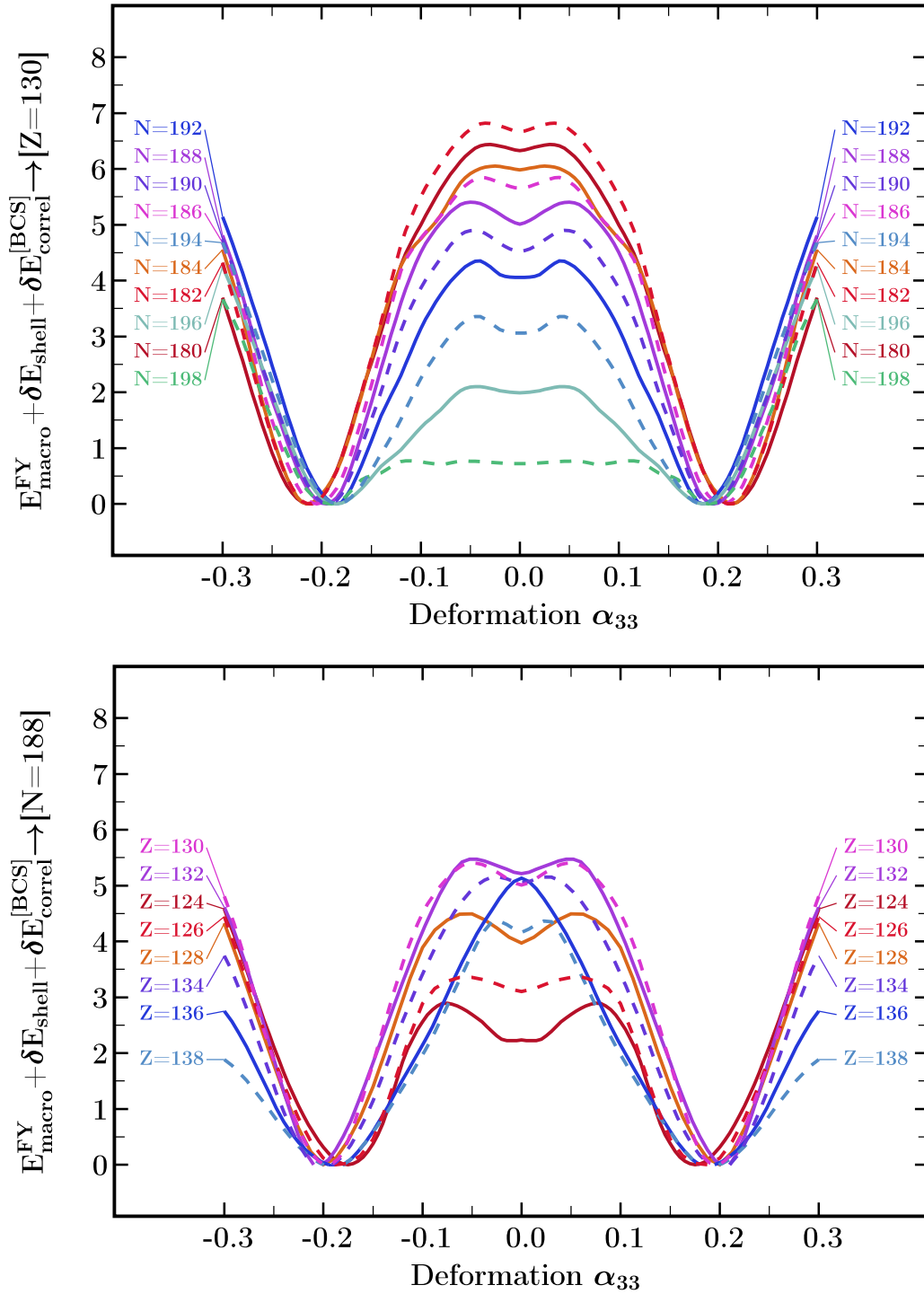


FIG. 10. Results analogous to those in the two preceding figures, the present collection focusing on the “hyper-deformed oblate” nuclei. Calculations predict an existence of the whole group of nuclei manifesting D_{3h} -symmetry minima at the quadrupole deformation $\alpha_{20} \approx -0.90$ (“hyper-deformed oblate”). The effects of the D_{3h} symmetry can be considered huge in the present case: The isotope with $N = 180$, upper panel, gains nearly 7 MeV with a_{33} varying between 0 and ± 0.20 , the deformation which can be considered significant in the context. (bottom panel) Analogous results for the proton number varying between 124 and 138 at fixed central neutron number, $N = 188$.

three different zones of increasing nuclear flatness, viz., at $\alpha_{20} \in [-0.10, -0.20]$, $\alpha_{20} \approx -0.50$ and $\alpha_{20} \approx -0.85$, here called “islands” and referred to as normal, super- and hyperdeformed, respectively—in addition to the fourth one corresponding to vanishing α_{20} , the latter discussed in detail

in Ref. [32] and thus not included here. All these nuclear structure elements were introduced employing the guideline examples, i.e., examples of nuclei in which the effects in questions appear as the strongest, possibly dominating. The latter nuclei are referred to as central, specified by their proton

and neutron numbers, Z_0 and N_0 . The decisive question is How these effects propagate from the central nucleus “in the middle of the island” down to the island’s shores.

In this section we present more systematically the evolution with varying Z and N of the symmetry-generating mechanisms from the centers to the outskirts of each given island. The graphical presentation technique used so far and based on the contour plotting had several advantages allowing to compare directly the competition of various shape effects at the same time or various families of shapes by adapting the particular projections used. But a big disadvantage in the present context consists in the needs of considerable space in the article. In this section we introduce a compromise replacing illustrations based on the contour-plot projections, by appropriately selected families of curves—thus loosing certain details. However, in this way the space-consuming maps are replaced by sets of curves like those presented in Fig. 7. In this way we obtain the possibility of comparing numerous nuclei at the same plot. Despite loosing certain details we gain in an overview in terms of the Z and N evolution of the structural behavior in a given mass zone.

The upper diagram in Fig. 8 illustrates the comparison of the total-energy curves for fixed central nucleus proton number, $Z_0 = 118$, while varying the neutron number around the central value $N_0 = 184$ —under the condition that all nuclei included, present a normal deformed oblate form. Comparison shows that the central nucleus gains nearly 3 MeV of potential energy while deforming from $\alpha_{33} = 0$ to $\alpha_{33} = \pm 0.08$. In comparison, the $N = 174$ isotope gains a little below 1 MeV only.

The partner-set of curves presented in Fig. 8, bottom, illustrates the structural evolution with varying proton numbers of the $N_0 = 184$ isotones. Incidentally, the strongest manifestation of the discussed symmetry corresponds to the similar gain of about 3 MeV of the energy for the α_{33} deformation varying from $\alpha_{33} = 0$ to $\alpha_{33} = \pm 0.08$.

Let us emphasize that the energy variations predicted by the present modeling are strong, since lowering energy by about 3 MeV may significantly strengthen the stability of the superheavy nuclei in question and thus increase the chances for the experimental identification.

Passing to the results related to the next island, Fig. 9, the one characterized by the presence of the superoblate $\alpha_{20} \approx -0.50$ components, one notices that the gain in energy accompanying the transition $\alpha_{33} = 0 \rightarrow \alpha_{33} = \pm 0.08$, is relatively modest but still non-negligible, of the order of 1.5 MeV for the most favorable cases.

The latter trend is significantly strengthened in the last island corresponding to the hyper-oblate shapes, cf. Fig. 10 (for the shape illustration, see Fig. 1) with $\alpha_{20} \approx -0.90$. Indeed, in the most favorable cases we note huge energy gains corresponding to about 7 MeV, when the D_{3h} -symmetric deformation reaches relatively large values of $\alpha_{33} \approx \pm 0.20$.

All the cases discussed can be seen as representing a number of common features:

- (i) In all the cases cited, there exist local potential-energy minima with nonvanishing α_{33} deformations, typically in the interval $\alpha_{33}^{\text{eq}} \in [0.10, 0.20]$.

- (ii) Similarly, in all the cases the nonvanishing α_{33} deformations are accompanied by nonvanishing quadrupole axial deformation component.
- (iii) Again in all the cases, the potential-energy minima are generated at the oblate shape configurations ($\alpha_{20}^{\text{eq}} < 0$) with no exceptions.
- (iv) By acquiring the D_{3h} -symmetry shapes the oblate hyper-deformed nuclei gain in the strongest manner, that is to say up to 7 MeV.

Let us emphasize that the discussed results are indicative for big numbers of nuclei. Indeed, whereas the illustrations were limited to the variations over N for the fixed Z_0 -central and vice versa, variations over Z for fixed N_0 -central, similar pictures apply for many other (Z, N) combinations, even if with less significant energy gains. This means that we are addressing the D_{3h} -symmetry effects in over 150 nuclei, out of which at least some can be populated in forthcoming experiments.

Let us return to the issue of an experimental identification of the discussed structures. Certain mechanisms could facilitate identification of predicted structures if more than one state or transition could be identified. For instance, hyperdeformed configurations are expected to generate very large moments of inertia and thus low rotational transition energies—even if population of such states via nuclear reactions could be difficult. Another, in a way most direct manner of identifying nuclear point-group symmetries, cf. recent Ref. [7], leads via detecting unique degeneracy patterns in the corresponding rotational spectra. Yet another mechanism, perhaps easier to observe, would be the decay into three comparable fragments (tripartition), as the result of the threefold symmetry, cf. Fig. 1.

IV. NUCLEAR PROPERTIES BASED ON SOLUTIONS OF COLLECTIVE SCHRÖDINGER EQUATION FOR D_{3h} VIBRATIONS

Experimental research in the domain of superheavy nuclei often encounters an extra difficulty, not necessarily present in the studies of lighter or not exotic nuclei: the difficulties in populating or detecting the presence of several transitions or states in the decay schemes. Indeed, in the research of superheavy nuclei, an identification of just one new state or transition can often be considered as a significant contribution to the progress.

In this article we discuss possible existence of superheavy nuclei satisfying D_{3h} symmetry in relatively broad sectors of the nuclear mass table. It has been shown in Ref. [7] using group theory methods that nuclear states with point-group symmetries can be identified through measurements of rotational bands predicted to contain numerous characteristic degenerate levels. The latter provide unique identification criteria if a sufficient number of such levels can be observed. It then becomes clear that in the domain of superheavy nuclei, this type of symmetry identification will not be straightforward to apply simply because of the very limited numbers of the observed transitions.

Consequently, it will be instructive to address the issue of possible presence of any other structure effects which could become the experimental signals of the symmetries of interest. A natural suggestion consists in exploring the theory of nuclear collective oscillations, which provides a number of specific spectroscopic features generated by the nuclear potentials with double or triple potential-energy minima separated by various types of barriers. The corresponding approach is necessarily based on the microscopic theory of nuclear collective inertia which provides methods of effective construction of the so-called inertia tensor, see below, needed to write down (and solve) the collective Schrödinger equation within the Bohr theory.

Recently a significant progress has been achieved in this domain via formulating new principles of nuclear adiabaticity—the latter serving as the underlying concept of microscopic theory of nuclear collective inertia, Ref. [33]. Significant mathematical improvements of the theory have been proposed allowing to totally remove the well-known instabilities of the previous formulations based on the perturbation theory and caused by the crossing of single-particle levels as functions of varying deformation. As the consequence, vanishing energy differences appearing in the denominators of certain mathematical expressions cause divergencies of the resulting inertia tensors with the corresponding impact on the solution of the collective Schrödinger equation.

In what follows we present, in a simplified manner, the nuclear collective Schrödinger equation and the characteristic features of its solutions in the context discussed in our article. The purpose is to identify certain quantum features of the collective solutions, which can become helpful in identification of predicted collective motion properties of the discussed superheavy nuclei. The mechanism of interest will be related to what is referred to in the literature as “parity doublets,” with often close-lying-, sometimes nearly degenerate levels—the type of information which can become very useful when trying to identify the sought symmetry manifestations.

Let us introduce a simplified notation according to which the spherical tensor notation, as in $\{\alpha_{\lambda\mu}\}$, will be abbreviated by $\alpha_{\lambda\mu} \leftrightarrow q^n$ and their full ensemble $\{q^n\} \leftrightarrow q$, the latter variables playing roles of *generalized coordinates* in analytical mechanics; here $n = 1, 2, \dots, d$ with d denoting the dimension of the considered space. With this simplified notation it will be instructive to recall the general form of a classical Lagrangian of the motion with $\{\dot{q}^n\}$ treated as generalized velocities. The corresponding Lagrangian has the general form

$$L(q, \dot{q}; \tau) = \sum_{m,n=1}^d \frac{1}{2} B_{nm}(q; \tau) \dot{q}^n \dot{q}^m - V(q), \quad (14)$$

in which position-dependent functions $B_{nm}(q; \tau)$ are generalized inertia coefficients forming a matrix referred to as inertia tensor; $V(q)$ will be identified with the nuclear potential energy here obtained using Strutinsky method. The advantage of the expression in Eq. (14) is that it allows us to apply directly the standard quantization procedures leading to the expression of the Laplacian Δ in the corresponding d -dimensional

curvilinear space

$$\Delta = \sum_{m,n=1}^d \frac{1}{\sqrt{|B|}} \frac{\partial}{\partial q^n} \left(\sqrt{|B|} B^{nm} \frac{\partial}{\partial q^m} \right), \quad (15)$$

where $|B|$ denotes the determinant of the matrix B_{nm} . The collective Schrödinger equation has the form

$$\hat{H}_{\text{col}} \Psi_{\text{col};i} = E_{\text{col};i} \Psi_{\text{col};i}, \quad (16)$$

in which the collective Hamiltonian is defined with the help of Eq. (15) by

$$\hat{H}_{\text{col}} = -\frac{\hbar^2}{2} \Delta + V(q). \quad (17)$$

The central information point in the present context is that Ref. [33] indicates how to construct in a realistic manner the nuclear inertia tensor, $B^{nm}(q)$, with the help of the phenomenological mean-field Hamiltonian; illustrations are presented in the cited reference. Therefore, the mass tensor can be considered known for all the calculations needed, even if obtained numerically after application of an algorithm, which is far from trivial.

The new derivation introduces a new realization of the adiabaticity concept addressing explicitly the timescales of the slow (collective) and the fast (single-nucleonic) motion together with a scale factor relating the two modes. Since components of the tensor of inertia are expressed with the help of matrix elements involving the derivatives of the mean-field Hamiltonian, the underlying microscopic information does not involve any new adjustable parameters. It has been demonstrated, as an illustration of the new approach, that it reproduces collective vibration energies 3_1^- , 2_1^+ , and 0_2^+ in the ^{208}Pb nucleus with the standard (unmodified) mean-field Hamiltonian. This latter result can be seen as very encouraging for the future large-scale applications of the new method.

However, the issue of solving collective Schrödinger equation of motion in multidimensional spaces like in the case of our project is yet another problem of high complexity requiring detailed solutions, usually treated on the case by case basis, for each nucleus of interest. This is a problem for another, specialized study, which is in progress and whose results will be published elsewhere. In what follows we will illustrate briefly characteristic *structural properties* of the lowest-energy collective-vibrational solutions using one-dimensional projections.

More precisely, the idea consists in formulating semiquantitative theory criteria of identifying signals coming from the collective oscillations of the nuclei with twin-minimum potential wells, without necessity of solving the full multidimensional Bohr model (which is the subject of an independent study). With this goal in mind we will show that the presence of some close-lying levels of opposite parities in experimental results at an excitation energy close to the top of the potential barrier separating the twin minima, cf. Fig. 11, can be used as an identifying signal. More details are formulated below.

We are interested in the problem of collective oscillatory motion associated with the potential-energy minima involving α_{33} deformation and possibly α_{20} partner one. As it turns out, certain properties of the lowest energy solutions can be

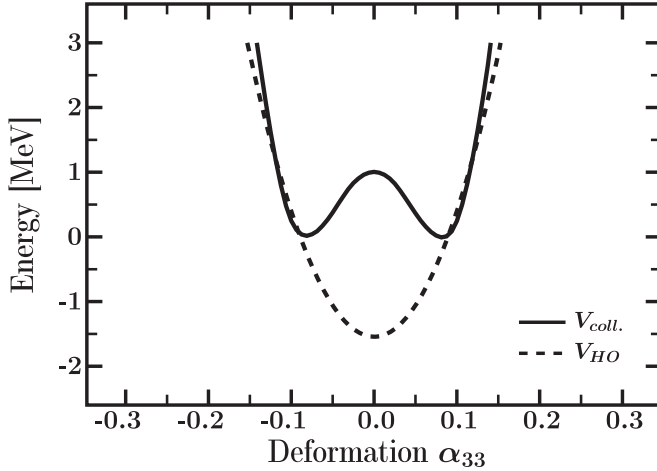


FIG. 11. An example of a one-dimensional projection of the double-minimum potential well together with the parabolic potential used to generate HO basis serving in solving the collective Schrödinger equation via diagonalization method. The parameters of the HO potential are adjusted to provide maximum overlap with the studied one.

examined using approximate separable forms of the potential: $V(\alpha_{20}, \alpha_{33}) \approx V_2(\alpha_{20}) + V_3(\alpha_{33})$. With this guideline in mind we are going to focus on the one-dimensional form of the collective Schrödinger equation obtained from the one in Eq. (17), projected on the $\alpha_{33} \leftrightarrow q$ axis. It can be shown that implied one-dimensional collective Schrödinger equation has the form

$$\left[-\frac{\hbar^2}{2} \left(\frac{1}{\sqrt{B(q)}} \frac{d}{dq} \right) \left(\frac{1}{\sqrt{B(q)}} \frac{d}{dq} \right) + V(q) \right] \Psi_i(q) = E_i \Psi_i(q), \text{ with } q = \alpha_{33}, \quad (18)$$

where $B(q)$ represents the position dependent “effective-mass parameter.” One can demonstrate that the solution of the above equation can be facilitated by an auxiliary transformation equivalent to changing the variables, leading to the new form of the equation with a constant effective inertia parameter.

Let us consider a double-minimum potential like the one in Fig. 11, representing a typical projection of the multi-dimensional potential-energy surface of a given nucleus on the α_{33} -deformation axis. To solve the corresponding one-dimensional Schrödinger equation we would need to know the realistic theory predictions for the inertia parameters like those calculated numerically in Ref. [33]. Instead, we will find out, how structural characteristics of solutions, such as wave functions, eigenenergies, most probable deformations, etc., are influenced—on a semiquantitative level—when the average inertia (constant mass parameter) increases.

It is well known from general quantum mechanics that there exist characteristic inter-relations among the lowest-lying solutions with double-well potentials, cf. Ref. [34] and references therein. They depend on the energy distance between the top of the potential barrier separating the twin minima and the lowest solution. We will illustrate the structure of the wave functions of the lowest vibration energies

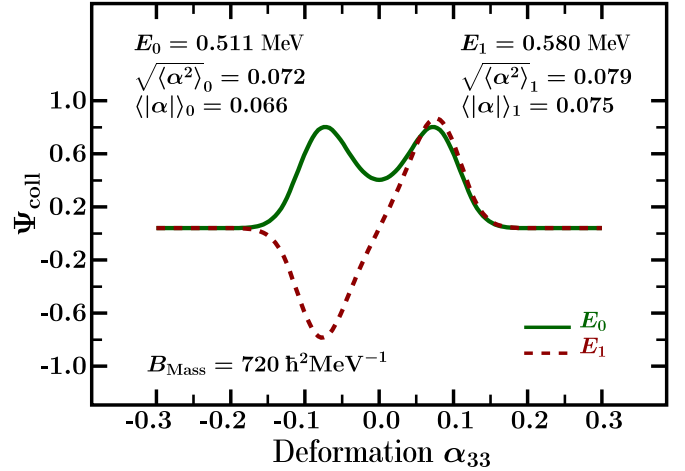


FIG. 12. Wave functions of the two lowest energy solutions of the collective Schrödinger equation, E_0 and E_1 , with the constant mass parameter, B_{Mass} , adjusted in such a way that E_0 is of the order of $1/2$ of the barrier (visible in Fig. 11) separating the twin minima. The meaning of the other symbols is discussed in the text.

comparing solution with energies lying markedly below the barrier top with those close to the top and finally, those lying markedly above the barrier. Another goal will be to estimate the dynamical equilibrium deformations.

Let us consider first what we call the “low-energy limit,” here defined by choosing the mass parameter, $B(q) \leftrightarrow B_{\text{Mass}}$, in such a way that the lowest-energy solution satisfies approximately $E_0 \sim (1/2)V_B$, where V_B denotes the barrier height separating the twin minima, cf. Fig. 11. The two wave functions corresponding to the lowest solutions $E_0 = 0.51$ MeV and $E_1 = 0.579$ MeV (with $B_{\text{Mass}} = 720\hbar^2 \text{MeV}^{-1}$) are illustrated in Figs. 12–14. Let us notice that the energies are nearly degenerate, and *both wave functions lead to the minima of the probability density functions at the origin of the reference*

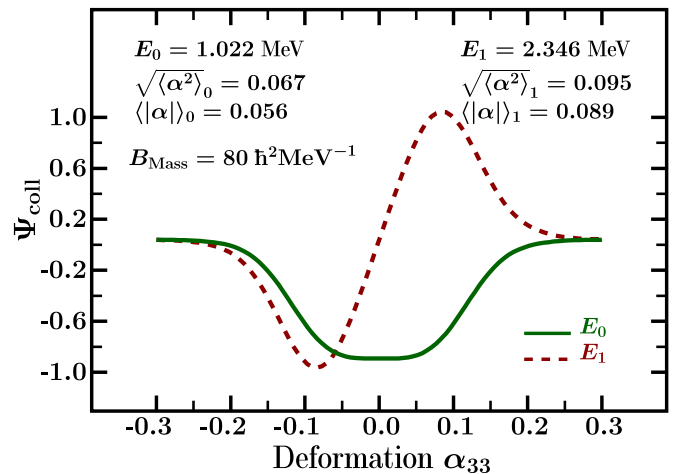


FIG. 13. Illustration analogous to the preceding figure but with the inertia parameter adjusted in such a way that E_0 is of the order of the barrier height separating the twin minima. For further comments see the text.

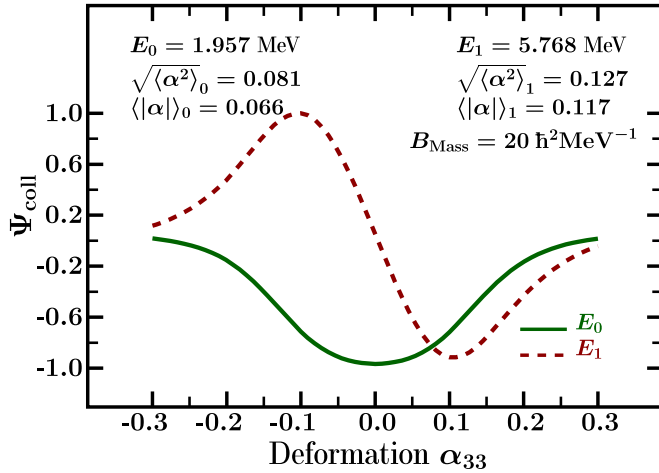


FIG. 14. Illustration analogous to the preceding figure but in this case with the inertia parameter adjusted in such a way that E_0 is of the order of the double of the barrier height separating the twin minima. For further comments see the text.

frame. Experimental identification of this situation would lead to the search of the opposite-parity doublet at the relatively low excitation energies.

As the next step we will compare analogous properties in the case of the higher-energy solutions, with the mass parameter adjusted in such a way that $E_0 \approx V_B$. This has been obtained by choosing $B_{\text{Mass}} = 80\hbar^2 \text{ MeV}^{-1}$. Let us notice that the splitting between the two lowest energies is incomparable with the one in the previous case, with E_1 more than double of the E_0 value in the present case. Also, the probability density ($\alpha\Psi^*\Psi$) behavior near the origin of the reference frame is different compared with the previous case: We notice the maximum for the Ψ_0 solution and the minimum for the Ψ_1 solution. Finally, the ground-state solution wave function has a one-extremum (probability shows a maximum) characteristic for the harmonic oscillator type solutions. Thus the experimental confirmation of the second scenario should correspond to relatively higher excitation energies and a significant splitting between E_0 and E_1 .

As the last example we have chosen what we call the “high-energy limit” with the $E_0 \sim 2V_B$. By setting $B_{\text{Mass}} = 20\hbar^2 \text{ MeV}^{-1}$, we arrive at $E_0 = 1.958 \text{ MeV}$, much lower compared with the first-excited state with $E_1 = 5.738 \text{ MeV}$. In contrast, the behavior of the two discussed wave functions is very similar to the previous case.

Finally let us pass to the discussion of the behavior of the so-called dynamical equilibrium (or most probable) deformations associated with the $\alpha_{33} \leftrightarrow q$ deformations. One of the often employed choices of the measure of such a most probable shape is by selecting the expected values of the corresponding variable:

$$\langle \alpha \rangle_{0,1} \stackrel{df.}{=} \int \Psi_{0,1}^*(\alpha) \alpha \Psi_{0,1}(\alpha) d\alpha. \quad (19)$$

However, one notices immediately that such a measure of the most probable deformation is unacceptable in the present context because Eq. (19) implies $\langle \alpha \rangle_0 \equiv 0$ for positive parity (E_0)

TABLE I. Example of an evolution of energies of D_{3h} -symmetry minima, here chosen as hyper-oblate $\alpha_{20} \approx -0.85$ configurations, for $N = 188$ isotones. The second column shows excitation energy above the ground-state minimum, vanishing values signifying that the D_{3h} minimum is the ground-state one. Columns 2, 3, and 4 show the equilibrium values of the deformations indicated. The last column gives the height of the potential barriers, V_B , separating the twin minima at a given α_{33} and $-\alpha_{33}$. In view of the discussion of the properties of the solutions of the Bohr collective model presented in this section, the displayed barrier heights can be seen as a guideline in anticipating semiquantitatively the presence of the parity doublets in the excitation patterns.

| $N = 188$ | D_{3h} minimum | | | Barrier | |
|-----------|------------------|---------------|---------------|---------|---------------|
| | Energy | α_{20} | α_{33} | | α_{40} |
| Z | | | | V_B | |
| 126 | 3.59 | -0.80 | 0.20 | 0.10 | 1.72 |
| 128 | 2.10 | -0.85 | 0.20 | 0.15 | 2.72 |
| 130 | 0.16 | -0.85 | 0.20 | 0.15 | 3.75 |
| 132 | 0.00 | -0.85 | 0.21 | 0.15 | 4.40 |
| 134 | 0.00 | -0.85 | 0.21 | 0.15 | 4.63 |
| 136 | 0.00 | -0.90 | 0.18 | 0.15 | 4.62 |

solutions with symmetric wave functions, whereas the laps of time spent by the system in the vicinity of the null-value deformation is maximum (the probability density function has the maximum at $\alpha = 0$).

We may consider two alternative measures of the most probable deformations used in the literature, the root-mean-square one defined by $(\langle \alpha^2 \rangle)^{1/2}$ for the two considered solutions

$$\langle \alpha^2 \rangle_{0,1} \stackrel{df.}{=} \int \Psi_{0,1}^*(\alpha) \alpha^2 \Psi_{0,1}(\alpha) d\alpha, \quad (20)$$

or the most probable absolute value

$$|\overline{\alpha}|_{0,1} \stackrel{df.}{=} \int \Psi_{0,1}^*(\alpha) |\alpha| \Psi_{0,1}(\alpha) d\alpha. \quad (21)$$

It turns out that both considered measures of the most probable deformation are close to each other, at least in the typical deformation ranges considered in this article. It follows from numerical calculations using definitions in Eqs. (20) and (21) that

$$|\overline{\alpha}|_{0,1} < \sqrt{\langle \alpha^2 \rangle_{0,1}}. \quad (22)$$

Calculations show that both measures of the dynamical-equilibrium shapes increase with increasing energy of the collective solutions.

Suppose, as a working hypothesis, that the octupole vibrations in the examined range of nuclei correspond to some typical value, for instance $E_{\text{vib}} \approx 1 \text{ MeV}$. Comparing the variation of the predicted barriers V_B with Z and N and following our supposition, we should be able to predict—even if in a semiquantitative manner—the expected structure of the lowest vibrational excitations. For instance, for relatively high barriers, which separate the twin minima, say $V_B \approx 2 \text{ MeV}$ or higher, the E_0 and E_1 energies are likely to lie lower or significantly lower than the top of the barrier. When this happens we should expect two nearly degenerate vibrational states of opposite parities. Identifying such states experimentally can

be used as a support of the D_{3h} -symmetry identification via collective D_{3h} vibrations.

Results presented in Table I give an example of a typical variation of the positions of the D_{3h} twin minima and of the separating barrier heights in a few selected nuclei for illustrative purposes. Extended list of results for all the nuclei and the competition between D_{3h} -symmetric hyperdeformed, superdeformed, and normal-deformed configurations and the other ones, mainly axially symmetric quadrupole deformed minima are collected in the summary tables in Appendix D.

V. SUMMARY AND CONCLUSIONS

In this article we study selected structural properties of heavy and superheavy nuclei predicted to manifest molecular D_{3h} point-group symmetry. In the range of the mass table discussed, this symmetry manifests itself via simultaneous presence of at least two nonvanishing multipole shape components. These are: an exotic, nonaxial octupole α_{33} deformation assuring the presence of a threefold symmetry axis among the nuclear symmetry elements and quadrupole $\alpha_{20} < 0$ axially symmetric deformation, adding an oblate shape component.

We begin the article by recalling briefly nuclear structure results published by various authors addressing nuclear potential-energy calculations for heavy and superheavy nuclei. Next we present in a compact manner our realization of the well-known macroscopic-microscopic method with a realistic phenomenological, so-called “universal” Woods-Saxon potential. Our approach takes into account the newest optimization of the Hamiltonian parameters employing inverse problem theory of applied mathematics to eliminate parametric correlations known to destroy the predictive power of mathematical modeling. This allows for a better control of uncertainties of the modeling and its predictive power.

The D_{3h} symmetry has been discussed together with a number of other nuclear point-group symmetries accompanying exotic octupole deformations α_{31} , α_{32} , and α_{33} in the recent Ref. [7]. The cited article shows, using point-group representation theory, that the most straightforward identification of the discussed nuclear symmetries leads via identification of the specific collective rotational band properties. The latter, in contrast with properties generated by the usual ellipsoidal rotors, manifests characteristic multiple degeneracies of rotational energies. Moreover, they involve both parities in a single band. Unfortunately, in the domain of superheavy nuclei, information about rotational bands is usually scarce. We introduce and discuss an alternative identification via collective oscillation properties of D_{3h} -symmetric nuclei employing collective Bohr model. We show that, in many cases, identification of nearly degenerate parity doublets may provide helpful support for symmetry identification.

We found three separate islands of nuclei with D_{3h} symmetry differing by their average $\alpha_{20} < 0$ deformations. We referred to the corresponding configurations in a rather descriptive manner as *archipelago of three islands*, each island determined by its typical α_{20} shape:

- (a) hyperdeformed oblate nuclei with $\alpha_{20} \approx -0.85$;
- (b) superdeformed oblate ones, with $\alpha_{20} \approx -0.50$; and

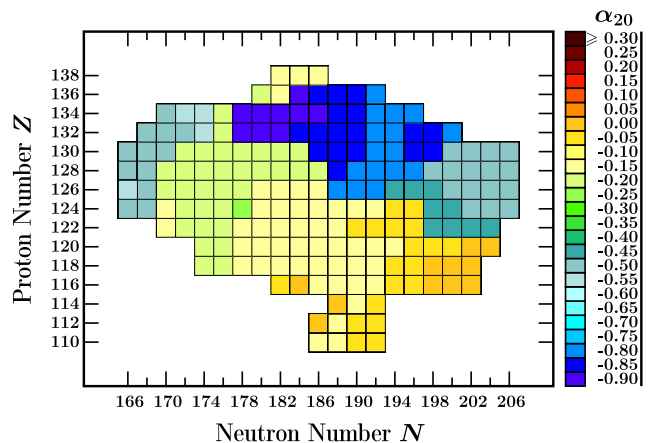


FIG. 15. Ground-state quadrupole deformation α_{20} for the nuclei studied. Observe that the largest (smallest-negative) oblate deformations, corresponding to $\alpha_{20} \approx -0.85$ or so are associated with $Z \in [128, 136]$ and $N \in [178, 198]$ nuclei. Comparison shows that they also correspond to the largest α_{33} (“strongest D_{3h} symmetry”) as seen from the following figure. The next in size, superdeformed oblate shapes correspond to nuclei with the proton numbers in the overlapping Z range, $Z \in [122, 134]$ and either $N < 174$ or $N > 196$. The normal-oblate deformed shapes dominate, as one can see by following the light-green, yellow, and orange in the diagram.

- (c) normal-deformed oblate with $\alpha_{20} \approx -0.20$ to -0.10 . For the reader’s convenience, typical discussed shapes of nuclear surfaces are illustrated in Fig. 1.

The word “islands” refers to groups of nuclei on the (Z, N) plane distributed in a nonoverlapping manner. Indeed, calculations show what we consider as a rather unusual occurrence pattern, that the quadrupole deformations of the local potential-energy minima are grouped as listed above “with nearly no cases in between.” This situation is illustrated in Fig. 15 where one can see that certain colors are totally

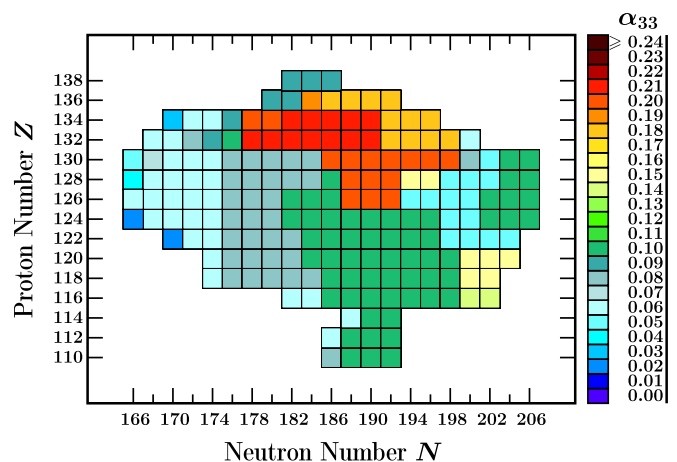


FIG. 16. Illustration of the repartition of the D_{3h} symmetry generating α_{33} shapes on the Z vs N plane. The corresponding partner α_{20} quadrupole deformations are illustrated in the analogous plot in Fig. 15. It deserves noticing that α_{33} , like all other deformations with odd λ satisfy the symmetry relation $E(-\alpha_{\lambda, \text{odd}, \mu}) = E(+\alpha_{\lambda, \text{odd}, \mu})$ so that the diagram is restricted to positive α_{33} values.

missing in the diagram, emphasizing separations and justifying the term *islands*.

The D_{3h} symmetry shapes are predicted to occur in a rectangle $110 \leq Z \leq 138$ and $166 \leq N \leq 206$. The corresponding repartition among the nuclei studied is illustrated in Fig. 16 indicating that the strongest manifestations of the D_{3h} symmetry correspond to $\alpha_{33} \approx \pm 0.20$, with $Z \in [128, 136]$, whereas the dominating α_{33} values, prevailing in majority of the presented nuclei are close to $\alpha_{33} \approx \pm 0.10$.

It turns out that the predicted exotic shapes dominate in the whole considered zone of the mass table bringing significant gains in terms of the binding energies thanks to the D_{3h} symmetry generated by the nonaxial octupole deformation α_{33} . It is worth emphasizing that energy gains due to D_{3h} symmetry approaches 7 to 8 MeV in several nuclei, and smaller but still significant energy gains in many others. As a consequence one should expect that some superheavy nuclei may exist, or be produced, thanks to the D_{3h} symmetry.

ACKNOWLEDGMENTS

J.D., H-L.W., and J.Y. would like to acknowledge partial support by the Polish National Science Centre under Contract No. 2016/21/B/ST2/01227. H-L.W. acknowledges partial support via the National Natural Science Foundation of China (Grant No. 11975209) and Physics Research and Development Program of Zhengzhou University (Grant No. 32410017). Partial support from the French-Polish collaboration COPIN, No. 04-113 and No. 05-119, and COPIGAL is acknowledged.

APPENDIX A: SELECTED GEOMETRICAL FEATURES OF THE MEAN-FIELD POTENTIAL

Even though spherical harmonics employed by us to parametrize the nuclear shapes belong to the best known special functions of applied mathematics, it will be instructive to recall a number of mathematical features, which are relatively seldom addressed in the literature, related to the description of nuclear geometry and combining various symmetries. With this goal in mind it will be important to recall the selection of the phase conventions and specific nuclear structure conventions related to the expansion coefficients $\{\alpha_{\lambda\mu}\}$ in the definition of $R(\vartheta, \varphi; \{\alpha_{\lambda\mu}\})$, of Eq. (3).

a. Limitations imposed by the nuclear surface equation. The nuclear surface is by definition a real function of its arguments,

$$R^*(\vartheta, \varphi; \{\alpha_{\lambda\mu}\}) = R(\vartheta, \varphi; \{\alpha_{\lambda\mu}\}). \quad (\text{A1})$$

The latter condition has direct implications resulting from the definition and properties of the spherical harmonics. Following Chap. 5 of the monograph [35], one finds

$$Y_{\lambda\mu}^*(\vartheta, \varphi) = (-1)^\mu Y_{\lambda-\mu}(\vartheta, \varphi). \quad (\text{A2})$$

One can easily show that, in order to satisfy Eq. (A1) it is sufficient to impose

$$\alpha_{\lambda\mu}^* = (-1)^\mu \alpha_{\lambda-\mu}. \quad (\text{A3})$$

b. Next limitation: Only real deformation parameters. Even though condition in Eq. (A1) can be satisfied using complex $\{\alpha_{\lambda\mu}\}$ in Eq. (A3)—in nuclear structure physics, the choice of the deformation parameters is restricted to the real values only, thus causing further limitations:

$$\alpha_{\lambda\mu}^* = \alpha_{\lambda\mu} \rightarrow \alpha_{\lambda\mu} = (-1)^\mu \alpha_{\lambda-\mu}. \quad (\text{A4})$$

Thanks to this limitation, results of the nuclear energy calculations can be presented in the form of two-dimensional “geographical maps,” used abundantly in the literature. Following Eq. (A2), to assure that for $\mu \neq 0$ nuclear surfaces remain real functions of their arguments we combine $\alpha_{\lambda\mu}$ and $\alpha_{\lambda-\mu}$ contributions as below:

$$\begin{aligned} & [\alpha_{\lambda\mu} Y_{\lambda\mu} + \alpha_{\lambda-\mu} Y_{\lambda-\mu}]^* \\ &= \underbrace{\alpha_{\lambda\mu}^* (-1)^\mu Y_{\lambda-\mu}}_{\alpha_{\lambda-\mu}} + \underbrace{\alpha_{\lambda-\mu}^* (-1)^\mu Y_{\lambda\mu}}_{\alpha_{\lambda\mu}} \\ &= \alpha_{\lambda-\mu} Y_{\lambda-\mu} + \alpha_{\lambda\mu} Y_{\lambda\mu} \leftrightarrow \text{real function}. \end{aligned} \quad (\text{A5})$$

Therefore, in what follows, these spherical harmonics will appear in pairs.

c. Odd- λ and mean-field inversion-symmetry breaking. With the inversion operator denoted \hat{P} we may write

$$\hat{P} : (\vartheta, \varphi) \rightarrow (\pi - \vartheta, \pi + \varphi) \rightarrow Y_{\lambda\mu} \rightarrow (-1)^\lambda Y_{\lambda\mu}, \quad (\text{A6})$$

cf. Sec. 5.5.2 of Ref. [35]. Consequently, for odd- λ , each couple of spherical harmonics in Eq. (A5) transforms under inversion as follows:

$$1 + [\alpha_{\lambda-\mu} Y_{\lambda-\mu} + \alpha_{\lambda\mu} Y_{\lambda\mu}] \xrightarrow{\hat{P}} 1 - [\alpha_{\lambda-\mu} Y_{\lambda-\mu} + \alpha_{\lambda\mu} Y_{\lambda\mu}], \quad (\text{A7})$$

and since the left-hand side is not equal to the right-hand side, the original surface before and after applying the inversion operator differs, cf. e.g., the monograph by Bohr and Mottelson, Ref. [36], page 16; compare with comments surrounding Eq. (A12) below.

d. \hat{S}_y -simplex: A universal symmetry for real $\{\alpha_{\lambda\mu}\}$. Elementary discrete symmetries such as inversion, single axis rotations through the angle of π , $\hat{R}_\kappa(\pi)$, where κ refers to x , y , and z axes—and their direct combinations giving rise to the plane reflections, $\hat{S}_\kappa \equiv \hat{P} \cdot \hat{R}_\kappa^{-1}$, were introduced to nuclear structure long ago, cf. e.g., Ref. [36], Sec. 4-2f, where spectroscopic consequences for the properties of rotational bands of some of these symmetries are discussed. After Ref. [37], we refer to the latter three operations as x , y , and z *simplexes*.

Below we will focus on the y simplex which, according to its very definition, implies a mirror reflection in the O_{xz} plane:

$$\hat{S}_y\{x, y, z\} = \hat{P} \hat{R}_y^{-1}\{x, y, z\} = \hat{P}\{-x, y, -z\} = \{x, -y, z\}, \quad (\text{A8})$$

or equivalently, in terms of spherical coordinates:

$$\hat{S}_y\{r, \vartheta, \varphi\} = \{r, \vartheta, -\varphi\}. \quad (\text{A9})$$

From elementary properties of spherical harmonics:

$$Y_{\lambda\mu}(\vartheta, -\varphi) = (-1)^\mu Y_{\lambda-\mu}(\vartheta, \varphi), \quad (\text{A10})$$

after Ref. [35], and consequently, for the real deformation parameters, any surface represented by Eq. (3) remains y

simplex invariant, since

$$\begin{aligned} & \hat{S}_y[\alpha_{\lambda\mu}Y_{\lambda\mu}(\vartheta, \varphi) + \alpha_{\lambda-\mu}Y_{\lambda-\mu}(\vartheta, \varphi)] \\ & \xrightarrow{\varphi \rightarrow -\varphi} \underbrace{\alpha_{\lambda\mu}(-1)^\mu Y_{\lambda-\mu}(\vartheta, \varphi)}_{\alpha_{\lambda-\mu}} + \underbrace{\alpha_{\lambda-\mu}(-1)^\mu Y_{\lambda\mu}(\vartheta, \varphi)}_{\alpha_{\lambda\mu}} \\ & = \alpha_{\lambda-\mu}Y_{\lambda-\mu}(\vartheta, \varphi) + \alpha_{\lambda\mu}Y_{\lambda\mu}(\vartheta, \varphi). \end{aligned} \quad (\text{A11})$$

e. Mean-field symmetry: $\hat{\mathcal{H}}_{\text{mf}}(-\alpha_{\lambda\mu}) = \hat{\mathcal{H}}_{\text{mf}}(+\alpha_{\lambda\mu})$. Under certain conditions, which will be specified below, nuclear surfaces defined by the deformation parameters $\alpha_{\lambda\mu}$ and their opposites $-\alpha_{\lambda\mu}$ represent exactly the same geometrical figure except for the orientation with respect to the original reference frame. As a consequence, the corresponding nuclear energies satisfy the symmetry

$$E(\alpha_{\lambda\mu}) = E(-\alpha_{\lambda\mu}), \quad (\text{A12})$$

which allows us to limit numerical calculations accordingly.

To be able to examine the conditions of applicability of these symmetry relations it will be instructive to examine elementary isometry operations such as reflections and rotations through a fixed angle about certain specific axes, $\hat{\mathcal{P}}$, $\hat{\mathcal{R}}_\kappa$, and $\hat{\mathcal{S}}_\kappa$ introduced earlier in this section. We begin by general considerations to arrive, as a particular case, at the octupole and hexadecapole shapes, which are of special interest in this article.

Let us emphasize that, according to the well-known group theory rules, the result of combining two or more group elements to construct another element may represent a symmetry of a given object, even if some or none of the combined operations alone are symmetry operations of the object considered. An example is provided by the y -simplex operation, which is the universal symmetry of any surface represented by real $\alpha_{\lambda\mu}$, cf. Eq. (A11). Indeed, $\hat{S}_y \equiv \hat{\mathcal{P}} \cdot \hat{\mathcal{R}}_y^{-1}$ is expressed with the help of inversion $\hat{\mathcal{P}}$, even though any odd- λ deformation breaks the inversion.

f. Reflection in \mathcal{O}_{xy} -plane: $z \rightarrow -z$ (case of z simplex). Following the above condition written using the spherical coordinates, we find $(\vartheta, \varphi) \rightarrow (\pi - \vartheta, \varphi)$, wherefrom:

$$Y_{\lambda\mu}(\vartheta, \varphi) \rightarrow Y_{\lambda\mu}(\vartheta - \pi, \varphi) = (-1)^{\lambda+\mu} Y_{\lambda\mu}(\vartheta, \varphi), \quad (\text{A13})$$

cf. Ref. [35], and it follows that for μ -even and λ -odd the spherical harmonics change signs so that

$$\begin{aligned} & [\alpha_{\lambda\mu}Y_{\lambda\mu}(\vartheta, \varphi) + \alpha_{\lambda-\mu}Y_{\lambda-\mu}(\vartheta, \varphi)]|_{(\vartheta \rightarrow -\vartheta, \alpha \rightarrow -\alpha)} \\ & = -\alpha_{\lambda\mu}[Y_{\lambda\mu}(\pi - \vartheta, \varphi)] - \alpha_{\lambda-\mu}[Y_{\lambda-\mu}(\pi - \vartheta, \varphi)] \\ & = [\alpha_{\lambda\mu}Y_{\lambda\mu}(\vartheta, \varphi) + \alpha_{\lambda-\mu}Y_{\lambda-\mu}(\vartheta, \varphi)], \end{aligned} \quad (\text{A14})$$

and by the same token showing the symmetry

$$E(\alpha_{\lambda\mu}) = E(-\alpha_{\lambda\mu}), \text{ for } \lambda\text{-odd and } \mu\text{-even.} \quad (\text{A15})$$

g. Reflection in \mathcal{O}_{xz} -plane: $y \rightarrow -y$ (case of y simplex). Since, for this transformation, in spherical coordinates we have $(\vartheta, \varphi) \rightarrow (\vartheta, -\varphi)$, one finds after Ref. [35]:

$$Y_{\lambda\mu}(\vartheta, \varphi) \rightarrow Y_{\lambda\mu}(\vartheta, -\varphi) = (-1)^\mu Y_{\lambda-\mu}(\vartheta, -\varphi), \quad (\text{A16})$$

and it follows that for odd- μ :

$$\begin{aligned} & [\alpha_{\lambda\mu}Y_{\lambda\mu} + \alpha_{\lambda-\mu}Y_{\lambda-\mu}]|_{(\varphi \rightarrow -\varphi, \alpha \rightarrow -\alpha)} \\ & = -\alpha_{\lambda\mu}[-Y_{\lambda-\mu}(\vartheta, -\varphi)] - \alpha_{\lambda-\mu}[-Y_{\lambda+\mu}(\vartheta, -\varphi)] \\ & = +\alpha_{\lambda\mu} \underbrace{Y_{\lambda-\mu}(\vartheta, -\varphi)}_{Y_{\lambda\mu}(\vartheta, \varphi)} + \alpha_{\lambda-\mu} \underbrace{Y_{\lambda+\mu}(\vartheta, -\varphi)}_{Y_{\lambda-\mu}(\vartheta, \varphi)} \\ & = [\alpha_{\lambda\mu}Y_{\lambda\mu} + \alpha_{\lambda-\mu}Y_{\lambda-\mu}], \end{aligned} \quad (\text{A17})$$

thus demonstrating the sought equality, from where one finds the symmetry

$$E(\alpha_{\lambda\mu}) = E(-\alpha_{\lambda\mu}) \forall \lambda, \mu\text{-odd.} \quad (\text{A18})$$

h. Particular application for octupole deformations. The general symmetry relations just obtained, when limited to the particular case $\lambda = 3$ imply that all the four octupole deformations $\alpha_{3;\mu=0,1,2,3}$ are good illustrative examples of discussed symmetry properties since

$$E(\alpha_{3\mu}) = E(-\alpha_{3\mu}), \quad \mu = 0, 1, 2, 3. \quad (\text{A19})$$

We focus next on the nuclei for which we find the equilibrium deformations with the shapes invariant under the D_{3h} -symmetry point-group.

APPENDIX B: ABOUT NUCLEAR D_{3h} GEOMETRY

Results of our macroscopic-microscopic calculations suggest that molecular point-group symmetry D_{3h} appears as the shape symmetry of many heavy and superheavy nuclei. As calculations show, the corresponding leading octupole deformation, α_{33} , is superposed with axial-symmetry negative quadrupole (oblate) and axial hexadecapole deformations. It will be instructive to present here some of the corresponding mathematical point-group-related elementary properties explicitly.

Point group D_{3h} is composed of 12 symmetry elements, the neutral one denoted \mathbf{I} and the leading one, threefold rotation operation denoted $\hat{\mathcal{C}}_3$, usually referred to as vertical. It is accompanied by a perpendicular plane reflection thus called horizontal, $\hat{\sigma}_h$, which can be identified with the \mathcal{O}_{xy} mirror, alternatively $z \rightarrow -z$ reflection or z simplex, and three perpendicular plane reflections referred to as vertical, $\hat{\sigma}_v^{(1)}$, $\hat{\sigma}_v^{(2)}$, and $\hat{\sigma}_v^{(3)}$. The latter are associated with planes passing through the vertical axis, one of them coinciding with the y -simplex or \mathcal{O}_{xz} -reflection operation. The list is completed by the three horizontal second-order rotation axes with operations traditionally denoted $\hat{\mathcal{U}}^{(1)}$, $\hat{\mathcal{U}}^{(2)}$, and $\hat{\mathcal{U}}^{(3)}$. All these symmetry elements can be collected as follows:

$$\begin{aligned} D_{3h} : \{ \hat{\mathcal{C}}_3, \hat{\mathcal{C}}_3^2, \hat{\mathcal{C}}_3^3 = \mathbf{I}, \hat{\mathcal{C}}_3 \circ \hat{\sigma}_h, \hat{\mathcal{C}}_3^2 \circ \hat{\sigma}_h, \hat{\mathcal{C}}_3^3 \circ \hat{\sigma}_h = \hat{\sigma}_h, \\ \hat{\mathcal{U}}^{(1)}, \hat{\mathcal{U}}^{(2)}, \hat{\mathcal{U}}^{(3)}, \hat{\sigma}_v^{(1)}, \hat{\sigma}_v^{(2)}, \hat{\sigma}_v^{(3)} \}. \end{aligned} \quad (\text{B1})$$

In the simplest variant, i.e., all deformations vanishing except for $\alpha_{33} \neq 0$, and recalling that $\alpha_{33} = -\alpha_{3-3}$, the corresponding D_{3h} -symmetric surface takes the form

$$R(\theta, \varphi; \alpha_{33}) \propto \{1 + \alpha_{33}[Y_{33}(\vartheta, \varphi) - Y_{3-3}(\vartheta, \varphi)]\}. \quad (\text{B2})$$

Introducing explicitly the spherical harmonics, Ref. [35], one finds

$$Y_{3\pm 3}(\vartheta, \varphi) = \mp \sqrt{35/64\pi} \sin^3 \vartheta e^{\pm 3i\varphi}. \quad (\text{B3})$$

According to the employed conventions and notation, the simplest D_{3h} -symmetric nuclear surface expression takes the form

$$R(\vartheta, \varphi; \alpha_{33}) = R_0 c(\alpha_{33}) [1 - a_{33} \sin^3 \vartheta \cos(3\varphi)]. \quad (\text{B4})$$

One can convince oneself by direct substitutions of the operations collected in Eq. (B1) that they indeed represent the symmetry operations of the nuclear shape with the simplest D_{3h} -symmetric surface definition of Eq. (B4).

As a simple illustration we may list a few particular examples such as the following ones:

$$\hat{C}_3 : \vartheta \rightarrow \vartheta \text{ and } \varphi \rightarrow \varphi + 2\pi/3, \quad (\text{B5})$$

or

$$\hat{U}^{(1)} : \vartheta \rightarrow \pi + \vartheta \text{ and } \varphi \rightarrow \varphi, \quad (\text{B6})$$

and further

$$\hat{\sigma}_v^{(1)} : \vartheta \rightarrow \vartheta \text{ and } \varphi \rightarrow 2\pi - \varphi, \quad (\text{B7})$$

or

$$\hat{C}_3 \circ \hat{\sigma}_h : \vartheta \rightarrow \pi - \vartheta \text{ and } \varphi \rightarrow \varphi + 2\pi/3, \quad (\text{B8})$$

all of them transforming $R(\vartheta, \varphi; \alpha_{33})$ into itself in a few elementary substitutions.

APPENDIX C: MESH SIZE AND CPU ESTIMATES FOR MULTIDIMENSIONAL GRID CALCULATIONS

Below we address the description of discrete meshes (grids) involving typically of the order of a few millions of deformation points in our typical nuclear potential-energy calculations. The projects of this type aim first of all at determining the presence of competing nuclear potential-energy minima and the implied shape-coexisting configurations together with their symmetries. The total nuclear energy expression is written down as a function of selected multipole deformations. Denoting their ensemble by $\{\alpha_{\lambda\mu}\} \leftrightarrow \alpha$, we may write:

$$E(Z, N) \leftrightarrow E(Z, N; \alpha) : \alpha_{\lambda\mu}^{\min} \leq \alpha_{\lambda\mu} \leq \alpha_{\lambda\mu}^{\max}. \quad (\text{C1})$$

The nuclear energies are tabulated using regular discrete meshes of points defined as follows:

$$\alpha_{\lambda\mu} = \alpha_{\lambda\mu}^{\min} + n\Delta\alpha_{\lambda\mu}; \quad n = 0, 1, \dots, N_{\lambda\mu}. \quad (\text{C2})$$

In our case of interest a typical deformation subspace is composed of four to five deformations selected within an ensemble composed of two quadrupole degrees of freedom, α_{20} and α_{22} , four octupole ones, α_{30} , α_{31} , α_{32} , and α_{33} , and hexadecapole ones, α_{40} and α_{42} .

1. Algorithm properties from the mesh sizes view point

It turns out that the mesh-size parameters, $N_{\lambda\mu}$, which are necessary for obtaining stable results are influenced by the

fact that the surface energy in the macroscopic energy expression depends rather sensitively on the multipolarity λ of the spherical harmonics. Generally, the bigger the λ the steeper the surface energy growth with an increase in the corresponding $\alpha_{\lambda\mu}$, implying that for the energy minimization purposes the corresponding deformation parameters can be kept within shorter variation intervals. According to our verifications of stability² with respect of increasing of the mesh sizes, in most of the meshes used we can pose for the quadrupole space

$$\alpha_{20}^{\min} = -1.2, \quad \alpha_{20}^{\max} = +0.8, \quad \text{and } \Delta\alpha_{20} = 0.025, \quad (\text{C3})$$

and

$$\alpha_{22}^{\min} = -0.8, \quad \alpha_{22}^{\max} = +0.8, \quad \text{and } \Delta\alpha_{22} = 0.025. \quad (\text{C4})$$

Similarly, for the octupole deformation subspace, we obtain stable results for $\mu = 0, 1, 2, 3$ with

$$\alpha_{3\mu}^{\min} = -0.4, \quad \alpha_{3\mu}^{\max} = +0.4, \quad \text{and } \Delta\alpha_{3\mu} = 0.025. \quad (\text{C5})$$

For odd multipolarity λ , either the y -simplex or the z -simplex symmetries apply, cf. Eqs. (A15) and (A18), respectively, therefore we may profit from the α sign-inversion symmetry $E(-\alpha_{\lambda\mu}) = E(+\alpha_{\lambda\mu})$. In this way we decrease considerably the numbers of needed mesh points, e.g., for 4-D octupole space we decrease the number of Hamiltonian calls by about the factor of eight.

For the typical hexadecapole deformations used we set

$$\alpha_{40}^{\min} = -0.3, \quad \alpha_{40}^{\max} = +0.3, \quad \text{and } \Delta\alpha_{40} = 0.025, \quad (\text{C6})$$

and similarly for α_{42} .

2. Algorithm performance in terms of CPU time costs

It will be instructive to estimate computing times for the typical mesh sizes, even if the results remain to an extent qualitative. As an example consider a 4-D mesh of deformations $(\alpha_{20}, \alpha_{22}, \alpha_{33}, \alpha_{40})$ with the numbers of node specifications $N_{20} = 81$, $N_{22} = 65$, $N_{33} = 33$, cf. Eqs. (C3)–(C5), and $N_{40} = 25$, Eq. (C6). Since for octupole deformation the sign-change symmetry $E(-\alpha_{\lambda=3\mu}) = E(+\alpha_{\lambda=3\mu})$ applies, we find that $N_{33} = 33 \rightarrow 32/2 + 1 = 17$, from where the total number of mesh points $N_{\text{mesh}} = N_{20}N_{22}N_{33}N_{40} = 2\,237\,625$, the number equal to the number of times we need to diagonalize the nuclear Hamiltonian.³

²Beginning with the interval $[\alpha_{\lambda\mu}^{\min}, \alpha_{\lambda\mu}^{\max}]$, we perform the total-energy calculations and produce the two-dimensional energy projections (maps) of interest. As the next step we increase the interval sizes and repeat the projections to make sure that, in the enlarged areas, there are no low-energy zones competing with the minima found earlier. Two situations may occur: Either in the enlarged zone of deformation space there are competing low-energy minima, in which case we enlarge the space, or there are none and we keep the last satisfactory $[\alpha_{\lambda\mu}^{\min}, \alpha_{\lambda\mu}^{\max}]$ intervals.

³Let us emphasize that the term ‘‘diagonalize nuclear Hamiltonian’’ hides several complex numerical procedures. To start, the Gauss integration algorithms are activated to define the Gauss nodes and weights for the integration over the three Cartesian variables $\{x, y, z\}$, bringing us to the number $N_x^{\text{Gauss}}N_y^{\text{Gauss}}N_z^{\text{Gauss}}$ i.e., about 100 000 to

In evaluating the computer work load for grids resembling the example above, let us assume that calculations for one deformation point take approximately a minute on a representative computer processor.⁴ With the $N_{\text{mesh}} = 2\,237\,625$, we need 37 294 hours to run the mesh on a single processor or, equivalently 1554 days, therefore 52 months or, finally, close to 4.5 years as a single processor job. In other words, with 10 000 to 50 000 processor installations we are at, typically, about 4 to 1 hour of CPU time per “typical 4-D mesh” discussed. Consequently, stepping up to five-dimensional (5-D) type meshes brings us to some days of the CPU waiting time for the physical result.

Needless to say, with a system composed of processors which are a factor f faster, we will shorten the CPU time approximately by a factor of f .

It is then easy to convince oneself that the dimension of the deformation space quickly becomes a prohibitive factor from the point of view of the CPU time and thus computing capacities. Indeed, suppose we wish to assure the stability of the total-energy results with respect to an increase in the number of multipoles in the nuclear surface definition, Eq. (3). As a practical illustration let us consider a six-dimensional (6-D) mesh of points composed of quadrupole and octupole deformations and apply the estimates of the space dimensions in terms of the number of mesh-points according to information given in Eqs. (C2)–(C6). With $N_{20} = 81$ and $N_{22} = 65$ as well as $N_{30} = N_{31} = N_{32} = N_{33} = 17(\leftarrow 0.8/0.025/2 + 1)$ we end up with $N_{\text{total}}^{6\text{-D}} = 439\,738\,065 \approx 0.5 \times 10^9$ mesh points. With a typical CPU performance of processors available, cf. footnote 4, our estimates bring us, approximately, to about 840 years execution time with a single processor or nearly a week for a 50 000-processor system.

According to Eq. (C6), extending further the above 6-D deformation space to an eleven-dimensional (11-D) one by introducing five extra hexadecapole degrees of freedom brings us to extending the number of nodes by including $N_{40} = N_{41} = N_{42} = N_{43} = N_{44} = 25$. However, according to Eq. (A18), for odd- μ , again the sign-inversion symmetry $E(-\alpha_{\lambda,\mu,\text{odd}}) = E(+\alpha_{\lambda,\mu,\text{odd}})$ applies so that $N_{41} = 25 \rightarrow 13$ and $N_{43} = 25 \rightarrow 13$. From there, working with 11-D space in place of the original 6-D one will need to multiply the preceding estimate of $N_{\text{total}}^{4\text{-D}}$ by the factor $2\,640\,625 \approx 2.6 \times 10^6$, i.e., equivalent to, approximately, $44\,154 \approx 4.4 \times 10^4$ years execution time with the 50 000-processor system as reference.

150 000 points at which the central potential and spin-orbit potentials need to be defined. For each $\{x, y, z\} \equiv \vec{r}$ the distance between \vec{r} and nuclear surface needs to be found using nonlinear minimization procedures, cf. Eqs. (5) and (7). With the Hamiltonian matrix of the dimensions typically 1000×1000 , of the order of 10^6 three-dimensional integrals need to be calculated. Finally, the so-obtained Hamiltonian matrices for the protons and the neutrons need to be diagonalized.

⁴The order of magnitude estimate proposed, which amounts to about 1 minute per deformation mesh-node, is based on performance of the processor selected—*Intel[®]Xeon[®] E5-2650 v3*. It happens to be representative for the processors available for our collaborations in Europe.

There are several advantages offered by the phenomenological mean-field techniques with the shapes parametrized with the help of basis expansions, for instance, employing a spherical harmonic basis, as discussed in the article. However, assuring the full stability (i.e., independence of the basis cutoff) of the predictions related among others to the competing shape minima and the separating barriers cannot be achieved by a direct increase in the size of the deformation space because of the accompanying too fast increase in the CPU requirements. Let us emphasize that the CPU time estimates presented in the above examples of realistic mesh sizes simply scale with the processor performance, see footnote 4. Consequently it becomes clear that alternative stability-testing approaches will be welcome.

3. Alternative manners of examining stability of the $\{Y_{\lambda\mu}\}$ basis

An alternative possibility of testing the stability in terms of increasing number of multipoles considered is a direct minimization of the mean-field potential energy, $E(Z, N; \alpha)$, using standard algorithms known in the literature such as steepest descent or conjugated gradient methods. Such tests can be performed in deformation spaces of dimensions, $\mathcal{N}_{\text{def}}^{\text{min}}$, bypassing significantly the limitations of five or six dimensions just discussed. This would allow for the sought stability tests concerning the numbers of the effectively obtained minima with an increase of the deformation-space dimension accompanying higher and higher multipolarities taken into account.

Let us notice that the mesh-type calculations allow for determining the presence of all local-energy minima in a considered deformation space. In contrast, the efficiency of the minimization methods in finding *all the local minima* depends strongly on how dense are the starting points selected by the algorithm. The minima found are often those close to the starting points of the iterative minimization process. Increasing such a density in many dimensions may strongly increase the CPU time demands. In the realistic applications, some among the sought minima may be missing and there is *defacto* no guarantee of finding all of them.

The method consists in gradually increasing the number of random restarts of the minimization routine sufficiently big number of times up to the saturation point and comparing the coordinates of the so obtained local minimum points with those obtained with the mesh algorithm. A few scenarios of testing with a given nucleus can be envisaged:

- (i) The number of minima in the $\mathcal{N}_{\text{def}}^{\text{min}}$ dimensional space is essentially the same as in the case of the mesh-algorithm with, say $\mathcal{N}_{\text{def}} = 6$, with small differences between the equilibrium deformations and the resulting energy values obtained with the two approaches, signifying that the final results are consistent and the dimensions of the deformation spaces of the mesh approach acceptable.
- (ii) The numbers of minima are the same, but the equilibrium values obtained by minimization in a richer space differ from the mesh results. It will be up to a physicist to decide whether differences are significant in the context, and how to adapt the dimensionality of the mesh space.

Any other test outcome showing unacceptable differences will signify a need of increasing deformation spaces for the application of the mesh-tabulation approach.

4. Acceleration of the mean-field performance using smooth dependence of eigenvalues on Z and N

There exist properties of nuclear phenomenological mean-field algorithms, which can be used for acceleration of the mesh calculations. One such property will be briefly recalled now addressing properties of the single-particle eigenenergies, e_v^{mf} , of the mean-field Hamiltonian treated as functions of the proton and neutron numbers.

Indeed, our phenomenological mean-field Hamiltonian presented in Sec. II A depends on the nucleon numbers, i.e., $\hat{\mathcal{H}}^{\text{mf}} = \hat{\mathcal{H}}^{\text{mf}}(Z, N; \alpha)$ and one may show that this type of the dependence is regular. *In principle* we should diagonalize the mean field Hamiltonian for each nucleus, i.e., for each Z and N pair, separately. However, one can show that the eigenenergies, $e_v^{\text{mf}}(Z, N; \alpha)$ are usually smooth functions of Z and N as well and, moreover, this dependence is regular (similar for all eigenvalues) and weak.

Consequently, the eigenvalues calculated for representative values of the proton and neutron numbers, say $Z = Z_0$ and $N = N_0$, can be used as an approximation without modifications, also for certain neighboring Z and N . It follows that if we are interested in nuclei with (Z, N) in the following sufficiently small intervals

$$Z \in [Z_{\min} < Z_0 < Z_{\max}], \quad \Delta Z \equiv Z_{\max} - Z_{\min}, \quad (\text{C7})$$

and

$$N \in [N_{\min} < N_0 < N_{\max}], \quad \Delta N \equiv N_{\max} - N_{\min}, \quad (\text{C8})$$

we will be able to produce the results for all

$$\mathcal{N}_{\text{nuc}} = (N_{\max} - N_{\min} + 1)(Z_{\max} - Z_{\min} + 1) \quad (\text{C9})$$

nuclei using the common set of eigenvalues at Z_0, N_0 . For that purpose we diagonalize the Hamiltonian for the “central

nucleus” with (Z_0, N_0) given by

$$Z_0 \sim \frac{1}{2}(Z_{\max} + Z_{\min}) \text{ and } N_0 \sim \frac{1}{2}(N_{\max} + N_{\min}), \quad (\text{C10})$$

and employ the Strutinsky method for all the (Z, N) -nuclei in Eqs. (C7) and (C8) using the Hamiltonian eigenvalues of the central nucleus. With, say, $\Delta Z \approx 10$ and $\Delta N \approx 10$, we can save the CPU time by a factor of $\Delta Z \Delta N \approx 10^2$.

APPENDIX D: LOWEST-ENERGY MINIMA, EQUILIBRIUM DEFORMATIONS, AND SEPARATING BARRIERS

In this section we provide a synthetic overview of the results of this article from the point of view of the two lowest potential-energy minima. The collection shown manifests two scenarios: Either both competing minima correspond to the D_{3h} symmetry, or one of them is D_{3h} symmetric and the other axially symmetric, oblate, the latter scenario dominates. In both cases the numerical values of the oblate quadrupole deformations may strongly differ, contributing to the variety of predicted scenarios.

Table II shows the competition between the D_{3h} -symmetry minima corresponding to the hyperdeformed configurations and the nearest competing minima some of which are also D_{3h} symmetric but, as it turns out, with $\alpha_{20} \in [-0.10, -0.45]$. Let us emphasize that in a big majority of the cases the potential barrier separating the two D_{3h} -symmetry twin-minima are larger or significantly larger than 2 MeV what suggests that in all these cases experimental signals of the configurations will be those of the low-lying parity doublet vibrational excitations.

Table III contains the results analogous to those in the preceding one, but with the D_{3h} -symmetric shapes superposed with the superdeformed (thus less flat) oblate quadrupole deformation components. Let us emphasize that for all but two cases the D_{3h} -symmetric minima represent the ground states. At the same time, and in contrast to the results of the preceding table, the potential barriers separating the twin-minima are negligibly small implying prediction of the absence of parity doublets and relatively highly positioned vibrational states.

TABLE II. D_{3h} -symmetry minima with α_{33} deformations superposed with hyperoblate quadrupole deformation components $\alpha_{20} \approx -0.85$. Column 2 gives the energy of the minimum above the ground-state energy, vanishing values signify that the D_{3h} -symmetric minimum has become ground-state. Columns 3, 4, and 5 give the static equilibrium deformations of the corresponding minima. Columns 6 and 7 show the potential barriers, $B_{D_{3h}}$ representing the separation of the twin minima with the D_{3h} -symmetry whereas B_{sep} gives the barrier separating the two considered lowest energy minima.

| $Z = 124$ | D_{3h} minimum | | | | Barrier | | Competing minimum | | | |
|-----------|------------------|---------------|---------------|---------------|--------------|------------------|-------------------|---------------|---------------|---------------|
| | Energy | α_{20} | α_{33} | α_{40} | $B_{D_{3h}}$ | B_{sep} | Energy | α_{20} | α_{33} | α_{40} |
| 188 | 4.84 | -0.80 | 0.18 | 0.10 | 1.06 | 6.46 | 0.00 | -0.10 | 0.10 | -0.05 |
| 190 | 4.14 | -0.80 | 0.18 | 0.10 | 1.85 | 5.99 | 0.00 | -0.10 | 0.10 | -0.05 |
| 192 | 3.75 | -0.80 | 0.16 | 0.12 | 2.02 | 5.35 | 0.00 | -0.10 | 0.10 | -0.05 |
| 194 | 3.77 | -0.80 | 0.15 | 0.12 | 2.17 | 5.54 | 0.00 | -0.05 | 0.10 | -0.02 |

TABLE II. (*Continued.*)

| N | D_{3h} minimum | | | Barrier | | Competing minimum | | | | |
|-----------|------------------|---------------|---------------|---------------|--------------|-------------------|--------|---------------|---------------|---------------|
| | Energy | α_{20} | α_{33} | α_{40} | $B_{D_{3h}}$ | B_{sep} | Energy | α_{20} | α_{33} | α_{40} |
| $Z = 126$ | | | | | | | | | | |
| 186 | 4.32 | -0.80 | 0.20 | 0.15 | 1.76 | 4.46 | 0.00 | -0.15 | 0.10 | -0.05 |
| 188 | 3.59 | -0.80 | 0.20 | 0.10 | 1.72 | 4.57 | 0.00 | -0.40 | 0.00 | -0.02 |
| 190 | 3.07 | -0.80 | 0.20 | 0.13 | 2.25 | 4.29 | 0.00 | -0.45 | 0.00 | -0.05 |
| 192 | 2.84 | -0.80 | 0.15 | 0.12 | 2.21 | 4.07 | 0.00 | -0.25 | 0.00 | -0.03 |
| 194 | 1.30 | -0.80 | 0.15 | 0.13 | 1.82 | 4.45 | 0.00 | -0.45 | 0.04 | -0.05 |
| 196 | 1.51 | -0.80 | 0.15 | 0.13 | 0.90 | 4.79 | 0.00 | -0.45 | 0.05 | -0.03 |
| $Z = 128$ | | | | | | | | | | |
| 186 | 2.35 | -0.85 | 0.20 | 0.15 | 2.38 | 3.82 | 0.00 | -0.20 | 0.10 | -0.05 |
| 188 | 2.10 | -0.85 | 0.20 | 0.15 | 2.72 | 3.97 | 0.00 | -0.40 | 0.00 | -0.02 |
| 190 | 1.53 | -0.80 | 0.20 | 0.13 | 2.93 | 3.59 | 0.00 | -0.40 | 0.00 | -0.07 |
| 192 | 1.29 | -0.80 | 0.20 | 0.12 | 2.84 | 3.27 | 0.00 | -0.25 | 0.00 | -0.03 |
| 194 | 1.73 | -0.80 | 0.15 | 0.13 | 1.77 | 3.21 | 0.00 | -0.25 | 0.00 | -0.03 |
| 196 | 2.04 | -0.80 | 0.15 | 0.13 | 1.32 | 3.70 | 0.00 | -0.25 | 0.00 | -0.05 |
| $Z = 130$ | | | | | | | | | | |
| 180 | 2.17 | -0.90 | 0.21 | 0.13 | 2.66 | 4.63 | 0.00 | -0.25 | 0.00 | 0.02 |
| 182 | 1.31 | -0.90 | 0.21 | 0.13 | 3.13 | 4.42 | 0.00 | -0.20 | 0.08 | -0.05 |
| 184 | 0.86 | -0.85 | 0.21 | 0.15 | 3.39 | 4.25 | 0.00 | -0.20 | 0.08 | -0.05 |
| 186 | 0.45 | -0.85 | 0.20 | 0.15 | 3.52 | 4.06 | 0.00 | -0.20 | 0.08 | -0.05 |
| 188 | 0.16 | -0.85 | 0.20 | 0.15 | 3.75 | 3.95 | 0.00 | -0.40 | 0.00 | -0.07 |
| 190 | 0.00 | -0.85 | 0.20 | 0.15 | 3.51 | 4.28 | 0.12 | -0.40 | 0.00 | -0.07 |
| 192 | 0.00 | -0.80 | 0.20 | 0.13 | 3.30 | 3.27 | 0.16 | -0.25 | 0.00 | -0.05 |
| 194 | 0.00 | -0.80 | 0.20 | 0.13 | 3.23 | 2.22 | 0.34 | -0.25 | 0.00 | -0.03 |
| 196 | 0.65 | -0.85 | 0.20 | 0.13 | 2.00 | 2.62 | 0.00 | -0.25 | 0.00 | -0.05 |
| 198 | 0.86 | -0.85 | 0.20 | 0.13 | 0.85 | 2.78 | 0.00 | -0.25 | 0.00 | -0.05 |
| $Z = 132$ | | | | | | | | | | |
| 176 | 0.39 | -0.90 | 0.21 | 0.12 | 1.98 | 2.81 | 0.00 | -0.20 | 0.09 | 0.00 |
| 178 | 0.00 | -0.90 | 0.21 | 0.12 | 2.69 | 2.87 | 0.06 | -0.25 | 0.00 | -0.03 |
| 180 | 0.00 | -0.90 | 0.21 | 0.12 | 3.68 | 3.80 | 0.29 | -0.25 | 0.00 | -0.03 |
| 182 | 0.00 | -0.90 | 0.21 | 0.12 | 4.33 | 5.81 | 0.97 | -0.35 | 0.00 | -0.06 |
| 184 | 0.00 | -0.90 | 0.21 | 0.12 | 4.15 | 5.28 | 0.88 | -0.40 | 0.00 | -0.09 |
| 186 | 0.00 | -0.85 | 0.21 | 0.15 | 4.35 | 5.27 | 1.19 | -0.40 | 0.00 | -0.09 |
| 188 | 0.00 | -0.85 | 0.21 | 0.15 | 4.40 | 5.73 | 1.34 | -0.40 | 0.00 | -0.09 |
| 190 | 0.00 | -0.85 | 0.21 | 0.15 | 4.51 | 5.83 | 1.35 | -0.40 | 0.00 | -0.09 |
| 192 | 0.00 | -0.80 | 0.18 | 0.15 | 3.83 | 5.77 | 1.60 | -0.35 | 0.00 | -0.09 |
| 194 | 0.00 | -0.80 | 0.18 | 0.15 | 3.07 | 5.16 | 1.20 | -0.25 | 0.00 | -0.06 |
| 196 | 0.00 | -0.80 | 0.18 | 0.15 | 2.05 | 4.33 | 0.75 | -0.25 | 0.00 | -0.06 |
| 198 | 0.00 | -0.80 | 0.18 | 0.15 | 1.01 | 3.42 | 0.41 | -0.25 | 0.00 | -0.06 |
| $Z = 134$ | | | | | | | | | | |
| 178 | 0.00 | -0.90 | 0.20 | 0.12 | 3.28 | 4.84 | 1.39 | -0.30 | 0.00 | -0.03 |
| 180 | 0.00 | -0.90 | 0.20 | 0.12 | 3.96 | 5.85 | 1.91 | -0.25 | 0.00 | -0.03 |
| 182 | 0.00 | -0.90 | 0.21 | 0.12 | 4.74 | 6.69 | 2.36 | -0.35 | 0.00 | -0.06 |
| 184 | 0.00 | -0.90 | 0.21 | 0.12 | 4.76 | 6.35 | 2.48 | -0.35 | 0.00 | -0.06 |
| 186 | 0.00 | -0.90 | 0.21 | 0.15 | 4.71 | 6.05 | 2.63 | -0.40 | 0.00 | -0.09 |
| 188 | 0.00 | -0.85 | 0.21 | 0.15 | 4.63 | 5.85 | 2.68 | -0.40 | 0.00 | -0.09 |
| 190 | 0.00 | -0.85 | 0.21 | 0.18 | 4.33 | 5.94 | 2.67 | -0.40 | 0.00 | -0.09 |
| 192 | 0.00 | -0.80 | 0.18 | 0.15 | 3.69 | 5.91 | 2.66 | -0.25 | 0.00 | -0.06 |
| 194 | 0.00 | -0.80 | 0.18 | 0.15 | 2.93 | 5.82 | 2.15 | -0.25 | 0.00 | -0.06 |
| 196 | 0.00 | -0.80 | 0.18 | 0.15 | 1.88 | 4.97 | 1.67 | -0.25 | 0.00 | -0.06 |

TABLE II. (*Continued.*)

| N | D_{3h} minimum | | | Barrier | | Competing minimum | | | | |
|-----------|------------------|---------------|---------------|---------------|--------------|-------------------|--------|---------------|---------------|---------------|
| | Energy | α_{20} | α_{33} | α_{40} | $B_{D_{3h}}$ | B_{sep} | Energy | α_{20} | α_{33} | α_{40} |
| $Z = 136$ | | | | | | | | | | |
| 184 | 0.00 | -0.90 | 0.20 | 0.12 | 5.48 | 7.65 | 4.21 | -0.35 | 0.00 | -0.06 |
| 186 | 0.00 | -0.90 | 0.18 | 0.18 | 5.69 | 6.44 | 4.63 | -0.40 | 0.00 | -0.09 |
| 188 | 0.00 | -0.90 | 0.18 | 0.15 | 4.62 | 6.51 | 4.40 | -0.40 | 0.00 | -0.09 |
| 190 | 0.00 | -0.85 | 0.18 | 0.18 | 4.53 | 6.67 | 4.45 | -0.40 | 0.00 | -0.09 |
| 192 | 0.00 | -0.85 | 0.18 | 0.18 | 3.07 | 6.50 | 4.36 | -0.40 | 0.00 | -0.06 |
| $Z = 138$ | | | | | | | | | | |
| 182 | 7.91 | -0.90 | 0.20 | 0.15 | 3.11 | 6.79 | 0.00 | -0.15 | 0.09 | -0.06 |
| 184 | 7.41 | -0.90 | 0.18 | 0.18 | 4.27 | 6.44 | 0.00 | -0.15 | 0.09 | -0.06 |
| 186 | 8.44 | -0.90 | 0.18 | 0.15 | 4.22 | 7.86 | 0.00 | -0.15 | 0.08 | -0.06 |
| 188 | 6.27 | -0.90 | 0.18 | 0.15 | 3.64 | 6.82 | 0.00 | -0.40 | 0.00 | -0.06 |

TABLE III. Analogous to the preceding table but with the D_{3h} -symmetry minima superposed with superoblate (rather than hyper-oblate) quadrupole $\alpha_{20} \approx -0.50$ configurations. Let us observe that some of those D_{3h} -symmetric shapes are in a direct competition with the hyperdeformed ones with axially symmetric quadrupole deformations corresponding to $\alpha_{20} \in [-0.80, -0.85]$.

| N | D_{3h} minimum | | | Barrier | | Competing minimum | | | | |
|-----------|------------------|---------------|---------------|---------------|--------------|-------------------|--------|---------------|---------------|---------------|
| | Energy | α_{20} | α_{33} | α_{40} | $B_{D_{3h}}$ | B_{sep} | Energy | α_{20} | α_{33} | α_{40} |
| $Z = 122$ | | | | | | | | | | |
| 198 | 0.00 | -0.45 | 0.05 | 0.02 | 0.02 | 1.83 | 0.63 | -0.25 | 0.00 | -0.02 |
| 200 | 0.00 | -0.45 | 0.05 | 0.02 | 0.11 | 2.22 | 0.86 | -0.25 | 0.00 | -0.02 |
| 202 | 0.00 | -0.50 | 0.10 | 0.00 | 0.26 | 2.70 | 1.66 | -0.25 | 0.00 | -0.02 |
| 204 | 0.00 | -0.50 | 0.10 | 0.00 | 0.29 | 2.62 | 1.98 | -0.25 | 0.00 | -0.02 |
| 206 | 0.00 | -0.50 | 0.10 | 0.00 | 0.27 | 2.58 | 2.17 | -0.25 | 0.00 | -0.02 |
| $Z = 124$ | | | | | | | | | | |
| 166 | 0.00 | -0.50 | 0.02 | 0.05 | 0.02 | 2.79 | 1.13 | -0.15 | 0.00 | 0.05 |
| 168 | 0.00 | -0.50 | 0.06 | 0.05 | 0.79 | 2.25 | 0.44 | -0.15 | 0.00 | 0.02 |
| 170 | 0.93 | -0.50 | 0.06 | 0.05 | 1.68 | 1.52 | 0.00 | -0.15 | 0.02 | 0.02 |
| 196 | 0.35 | -0.45 | 0.05 | 0.00 | 0.53 | 1.85 | 0.00 | -0.25 | 0.00 | -0.02 |
| 198 | 0.00 | -0.45 | 0.05 | 0.02 | 0.39 | 2.17 | 0.28 | -0.25 | 0.00 | -0.02 |
| 200 | 0.00 | -0.45 | 0.05 | 0.02 | 0.49 | 2.42 | 0.86 | -0.25 | 0.00 | -0.02 |
| 202 | 0.00 | -0.50 | 0.10 | 0.00 | 1.22 | 2.70 | 1.50 | -0.25 | 0.00 | -0.02 |
| 204 | 0.00 | -0.50 | 0.10 | 0.00 | 1.30 | 3.09 | 2.18 | -0.25 | 0.00 | -0.02 |
| 206 | 0.00 | -0.50 | 0.10 | 0.00 | 1.21 | 3.46 | 2.72 | -0.25 | 0.00 | -0.02 |
| $Z = 126$ | | | | | | | | | | |
| 166 | 0.00 | -0.50 | 0.06 | 0.05 | 0.02 | 3.58 | 1.60 | -0.20 | 0.00 | 0.05 |
| 168 | 0.00 | -0.50 | 0.06 | 0.05 | 0.52 | 2.56 | 0.78 | -0.15 | 0.00 | 0.02 |
| 194 | 0.00 | -0.45 | 0.04 | -0.06 | 1.03 | 4.45 | 1.30 | -0.80 | 0.15 | 0.13 |
| 196 | 0.00 | -0.45 | 0.06 | -0.03 | 1.12 | 4.79 | 1.51 | -0.80 | 0.15 | 0.13 |
| 198 | 0.00 | -0.50 | 0.05 | 0.02 | 0.77 | 1.95 | 0.50 | -0.25 | 0.00 | -0.05 |
| 200 | 0.00 | -0.50 | 0.05 | 0.00 | 0.69 | 2.24 | 0.13 | -0.25 | 0.00 | -0.05 |
| 202 | 0.00 | -0.50 | 0.05 | 0.00 | 0.66 | 2.52 | 0.69 | -0.25 | 0.00 | -0.04 |
| 204 | 0.00 | -0.50 | 0.10 | 0.00 | 0.63 | 2.90 | 1.26 | -0.25 | 0.00 | -0.03 |
| 206 | 0.00 | -0.50 | 0.10 | 0.02 | 0.61 | 3.33 | 1.86 | -0.25 | 0.00 | -0.02 |
| $Z = 128$ | | | | | | | | | | |
| 166 | 0.00 | -0.50 | 0.04 | 0.07 | 0.05 | 4.53 | 1.89 | -0.20 | 0.00 | 0.02 |
| 168 | 0.00 | -0.50 | 0.07 | 0.07 | 0.42 | 3.55 | 1.90 | -0.20 | 0.00 | 0.02 |
| 170 | 0.00 | -0.50 | 0.06 | 0.07 | 0.33 | 2.38 | 1.82 | -0.20 | 0.00 | 0.02 |
| 198 | 0.00 | -0.50 | 0.05 | -0.05 | 1.31 | 3.69 | 2.04 | -0.80 | 0.15 | 0.13 |
| 200 | 0.00 | -0.50 | 0.05 | 0.00 | 0.26 | 1.18 | 0.24 | -0.80 | 0.00 | 0.12 |
| 202 | 0.00 | -0.50 | 0.05 | 0.00 | 0.34 | 1.43 | 0.59 | -0.85 | 0.00 | 0.12 |

TABLE III. (Continued.)

| N | D_{3h} minimum | | | | Barrier | | Competing minimum | | | |
|-----------|------------------|---------------|---------------|---------------|--------------|-----------|-------------------|---------------|---------------|---------------|
| | Energy | α_{20} | α_{33} | α_{40} | $B_{D_{3h}}$ | B_{sep} | Energy | α_{20} | α_{33} | α_{40} |
| 204 | 0.00 | -0.50 | 0.10 | 0.00 | 0.42 | 1.77 | 0.64 | -0.85 | 0.00 | 0.13 |
| 206 | 0.00 | -0.50 | 0.10 | 0.05 | 0.41 | 2.41 | 0.38 | -0.85 | 0.00 | 0.13 |
| $Z = 130$ | | | | | | | | | | |
| 166 | 0.00 | -0.50 | 0.04 | 0.07 | 0.05 | 4.53 | 1.89 | -0.20 | 0.00 | 0.02 |
| 168 | 0.00 | -0.50 | 0.07 | 0.07 | 0.42 | 3.55 | 1.90 | -0.20 | 0.00 | 0.02 |
| 170 | 0.00 | -0.50 | 0.06 | 0.07 | 0.33 | 2.38 | 1.82 | -0.20 | 0.00 | 0.02 |
| 200 | 0.00 | -0.50 | 0.05 | 0.00 | 0.26 | 1.18 | 0.24 | -0.80 | 0.00 | 0.12 |
| 202 | 0.00 | -0.50 | 0.05 | 0.00 | 0.34 | 1.43 | 0.59 | -0.85 | 0.00 | 0.12 |
| 204 | 0.00 | -0.50 | 0.10 | 0.00 | 0.42 | 1.77 | 0.64 | -0.85 | 0.00 | 0.13 |
| 206 | 0.00 | -0.50 | 0.10 | 0.05 | 0.41 | 2.41 | 0.38 | -0.85 | 0.00 | 0.13 |
| $Z = 132$ | | | | | | | | | | |
| 168 | 0.00 | -0.50 | 0.06 | 0.06 | 0.05 | 3.51 | 2.36 | -0.25 | 0.06 | 0.00 |
| 170 | 0.00 | -0.50 | 0.06 | 0.07 | 0.03 | 2.61 | 1.38 | -0.20 | 0.06 | 0.02 |
| 172 | 0.00 | -0.55 | 0.08 | 0.06 | 0.28 | 2.88 | 0.24 | -0.20 | 0.06 | 0.00 |
| 174 | 0.00 | -0.55 | 0.09 | 0.09 | 0.29 | 2.24 | 0.30 | -0.20 | 0.06 | 0.00 |
| $Z = 134$ | | | | | | | | | | |
| 170 | 0.00 | -0.50 | 0.06 | 0.07 | 0.17 | 3.47 | 2.44 | -0.30 | 0.03 | 0.02 |
| 172 | 0.00 | -0.55 | 0.06 | 0.06 | 0.41 | 3.42 | 0.24 | -0.20 | 0.06 | 0.00 |
| 174 | 0.00 | -0.55 | 0.06 | 0.09 | 0.50 | 3.97 | 0.30 | -0.20 | 0.06 | 0.00 |
| 176 | 0.61 | -0.55 | 0.10 | 0.00 | 1.01 | 2.50 | 0.00 | -0.20 | 0.09 | 0.00 |

Tables IV and V present the results analogous to those before but here focusing on the minima with the normal deformed oblate shape quadrupole contributions.

TABLE IV. Similar to the preceding table but with the D_{3h} -symmetry minima combined with the normal-oblate quadrupole $\alpha_{20} \approx -0.20$ components, with $Z \in [110, 120]$.

| N | D_{3h} minimum | | | | Barrier | | Competing minimum | | | |
|-----------|------------------|---------------|---------------|---------------|--------------|-----------|-------------------|---------------|---------------|---------------|
| | Energy | α_{20} | α_{33} | α_{40} | $B_{D_{3h}}$ | B_{sep} | Energy | α_{20} | α_{33} | α_{40} |
| $Z = 110$ | | | | | | | | | | |
| 186 | 0.00 | -0.10 | 0.08 | -0.02 | 1.51 | 2.98 | 0.12 | 0.35 | 0.00 | 0.00 |
| 188 | 0.00 | -0.10 | 0.10 | -0.02 | 1.89 | 1.37 | 1.20 | -0.40 | 0.00 | -0.05 |
| 190 | 0.00 | -0.05 | 0.10 | -0.02 | 2.67 | 1.80 | 1.39 | -0.40 | 0.00 | -0.05 |
| 192 | 0.00 | -0.05 | 0.10 | -0.02 | 3.11 | 2.08 | 1.84 | -0.40 | 0.00 | -0.05 |
| $Z = 112$ | | | | | | | | | | |
| 186 | 0.00 | 0.00 | 0.06 | -0.02 | 1.05 | 1.38 | 1.06 | -0.35 | 0.00 | -0.02 |
| 188 | 0.00 | -0.10 | 0.10 | -0.02 | 1.35 | 1.38 | 0.96 | -0.40 | 0.00 | -0.05 |
| 190 | 0.00 | -0.05 | 0.10 | -0.02 | 1.68 | 1.44 | 0.89 | -0.40 | 0.00 | -0.05 |
| 192 | 0.00 | -0.05 | 0.10 | -0.02 | 2.13 | 1.70 | 1.30 | -0.40 | 0.00 | -0.02 |
| $Z = 114$ | | | | | | | | | | |
| 188 | 0.00 | 0.00 | 0.06 | -0.02 | 0.95 | 1.26 | 0.72 | -0.40 | 0.00 | -0.02 |
| 190 | 0.00 | -0.10 | 0.10 | -0.02 | 1.10 | 1.34 | 0.60 | -0.40 | 0.00 | -0.02 |
| 192 | 0.00 | -0.05 | 0.10 | -0.02 | 1.03 | 1.19 | 0.69 | -0.40 | 0.00 | -0.02 |
| $Z = 116$ | | | | | | | | | | |
| 182 | 0.00 | -0.05 | 0.06 | -0.02 | 0.23 | 1.69 | 0.54 | -0.15 | 0.08 | -0.02 |
| 184 | 0.00 | 0.00 | 0.06 | -0.00 | 0.30 | 2.52 | 1.13 | -0.15 | 0.08 | -0.02 |
| 186 | 0.00 | -0.15 | 0.10 | -0.02 | 1.55 | 1.84 | 1.67 | -0.40 | 0.00 | -0.02 |
| 188 | 0.00 | -0.10 | 0.10 | -0.02 | 1.60 | 1.05 | 0.49 | -0.40 | 0.00 | -0.02 |

TABLE IV. (*Continued.*)

| N | D_{3h} minimum | | | Barrier | | Competing minimum | | | | |
|-----------|------------------|---------------|---------------|---------------|--------------|-------------------|--------|---------------|---------------|---------------|
| | Energy | α_{20} | α_{33} | α_{40} | $B_{D_{3h}}$ | B_{sep} | Energy | α_{20} | α_{33} | α_{40} |
| 190 | 0.00 | -0.10 | 0.10 | -0.05 | 1.78 | 1.22 | 0.35 | -0.40 | 0.00 | -0.02 |
| 192 | 0.00 | -0.10 | 0.10 | -0.05 | 1.46 | 0.99 | 0.18 | -0.40 | 0.00 | -0.02 |
| 194 | 0.00 | -0.05 | 0.10 | -0.02 | 2.22 | 1.30 | 0.25 | -0.40 | 0.00 | 0.00 |
| 196 | 0.00 | -0.05 | 0.10 | 0.00 | 2.19 | 1.02 | 0.19 | -0.40 | 0.00 | 0.00 |
| $Z = 118$ | | | | | | | | | | |
| 174 | 0.00 | -0.20 | 0.06 | 0.05 | 0.86 | 2.95 | 1.97 | -0.35 | 0.00 | 0.02 |
| 176 | 0.00 | -0.20 | 0.08 | 0.02 | 0.74 | 2.51 | 1.85 | -0.35 | 0.00 | 0.02 |
| 178 | 0.00 | -0.15 | 0.08 | 0.00 | 1.25 | 1.79 | 1.56 | -0.35 | 0.00 | 0.00 |
| 180 | 0.00 | -0.15 | 0.08 | -0.02 | 1.02 | 1.82 | 0.21 | -0.35 | 0.00 | 0.05 |
| 182 | 0.00 | -0.15 | 0.08 | -0.02 | 1.07 | 1.99 | 0.96 | -0.35 | 0.04 | 0.05 |
| 184 | 0.00 | -0.15 | 0.08 | -0.05 | 0.50 | 1.63 | 0.59 | 0.00 | 0.00 | 0.00 |
| 186 | 0.00 | -0.15 | 0.10 | -0.02 | 1.10 | 1.39 | 0.97 | -0.40 | 0.00 | -0.02 |
| 188 | 0.00 | -0.10 | 0.10 | -0.02 | 1.17 | 1.15 | 0.21 | -0.40 | 0.00 | -0.02 |
| 190 | 0.00 | -0.10 | 0.10 | -0.05 | 1.36 | 1.32 | 0.64 | -0.40 | 0.00 | -0.02 |
| 192 | 0.00 | -0.10 | 0.10 | -0.02 | 0.44 | 1.30 | 0.18 | -0.40 | 0.00 | 0.00 |
| 194 | 0.00 | -0.05 | 0.10 | -0.02 | 0.32 | 1.25 | 0.72 | -0.40 | 0.00 | 0.00 |
| 196 | 0.00 | -0.05 | 0.10 | 0.00 | 0.32 | 1.16 | 0.66 | -0.40 | 0.00 | 0.00 |
| 198 | 0.00 | 0.00 | 0.10 | 0.00 | 0.42 | 1.09 | 0.57 | -0.40 | 0.00 | 0.02 |
| 200 | 0.00 | 0.00 | 0.15 | 0.02 | 0.93 | 1.11 | 0.31 | -0.45 | 0.00 | 0.02 |
| 202 | 0.00 | 0.00 | 0.15 | 0.02 | 0.98 | 1.34 | 0.22 | -0.45 | 0.00 | 0.02 |
| $Z = 120$ | | | | | | | | | | |
| 174 | 0.00 | -0.20 | 0.06 | 0.02 | 0.89 | 9.96 | 1.49 | 0.40 | 0.00 | 0.05 |
| 176 | 0.00 | -0.20 | 0.08 | 0.02 | 0.65 | 9.22 | 0.94 | 0.40 | 0.00 | 0.05 |
| 178 | 0.00 | -0.15 | 0.08 | 0.00 | 0.15 | 9.66 | 0.63 | 0.40 | 0.00 | 0.00 |
| 180 | 0.00 | -0.15 | 0.08 | -0.02 | 2.01 | 1.65 | 0.21 | -0.25 | 0.00 | -0.02 |
| 182 | 0.00 | -0.15 | 0.08 | -0.02 | 2.07 | 1.22 | 1.20 | -0.25 | 0.04 | 0.05 |
| 184 | 0.00 | -0.15 | 0.08 | -0.05 | 1.81 | 1.94 | 1.81 | 0.00 | 0.00 | 0.00 |
| 186 | 0.00 | -0.15 | 0.10 | -0.05 | 1.38 | 2.08 | 1.07 | -0.40 | 0.00 | 0.00 |
| 188 | 0.00 | -0.10 | 0.10 | -0.05 | 0.87 | 0.96 | 0.63 | -0.40 | 0.00 | -0.02 |
| 190 | 0.00 | -0.10 | 0.10 | -0.05 | 0.91 | 1.23 | 0.20 | -0.40 | 0.00 | -0.02 |
| 192 | 0.00 | -0.10 | 0.10 | -0.02 | 0.80 | 1.41 | 0.57 | -0.40 | 0.00 | 0.00 |
| 194 | 0.00 | -0.10 | 0.10 | -0.02 | 0.66 | 1.49 | 0.68 | -0.20 | 0.00 | -0.02 |
| 196 | 0.00 | -0.05 | 0.10 | 0.00 | 0.77 | 2.04 | 0.52 | -0.20 | 0.00 | 0.00 |
| 198 | 0.00 | -0.05 | 0.10 | 0.00 | 1.25 | 2.15 | 0.63 | -0.25 | 0.00 | -0.02 |
| 200 | 0.00 | -0.05 | 0.15 | 0.02 | 1.37 | 2.03 | 0.46 | -0.25 | 0.00 | -0.02 |
| 202 | 0.00 | 0.00 | 0.15 | 0.02 | 1.96 | 2.98 | 0.65 | -0.25 | 0.00 | 0.00 |
| 204 | 0.00 | 0.00 | 0.15 | 0.02 | 0.72 | 2.97 | 1.74 | -0.45 | 0.00 | 0.02 |

TABLE V. Follow-up of the preceding table for $Z \in [122, 138]$.

| N | D_{3h} minimum | | | Barrier | | Competing minimum | | | | |
|-----|------------------|---------------|---------------|---------------|--------------|-------------------|--------|---------------|---------------|---------------|
| | Energy | α_{20} | α_{33} | α_{40} | $B_{D_{3h}}$ | B_{sep} | Energy | α_{20} | α_{33} | α_{40} |
| 170 | 0.00 | -0.15 | 0.02 | 0.02 | 0.03 | 7.38 | 0.82 | 0.40 | 0.00 | 0.05 |
| 172 | 0.00 | -0.20 | 0.06 | 0.02 | 0.73 | 8.91 | 0.84 | 0.40 | 0.00 | 0.05 |
| 174 | 0.00 | -0.20 | 0.06 | 0.02 | 0.95 | 10.36 | 0.94 | 0.40 | 0.04 | 0.05 |
| 176 | 0.00 | -0.20 | 0.08 | 0.00 | 0.74 | 10.08 | 0.35 | 0.40 | 0.04 | 0.05 |
| 178 | 0.00 | -0.15 | 0.08 | 0.02 | 0.55 | 9.74 | 0.32 | 0.40 | 0.00 | 0.00 |
| 180 | 0.00 | -0.15 | 0.08 | -0.02 | 0.06 | 1.41 | 0.06 | -0.25 | 0.00 | -0.05 |
| 182 | 0.00 | -0.15 | 0.08 | -0.02 | 1.06 | 2.02 | 1.06 | -0.25 | 0.04 | 0.05 |

TABLE V. (Continued.)

| N | D_{3h} minimum | | | Barrier | | Competing minimum | | | | |
|-----------|------------------|---------------|---------------|---------------|--------------|-------------------|--------|---------------|---------------|---------------|
| | Energy | α_{20} | α_{33} | α_{40} | $B_{D_{3h}}$ | B_{sep} | Energy | α_{20} | α_{33} | α_{40} |
| 184 | 0.00 | -0.15 | 0.10 | -0.05 | 1.99 | 2.67 | 2.34 | -0.40 | 0.00 | 0.02 |
| 186 | 0.00 | -0.15 | 0.10 | -0.05 | 1.38 | 1.49 | 0.86 | -0.40 | 0.00 | 0.02 |
| 188 | 0.00 | -0.10 | 0.10 | -0.05 | 1.03 | 1.06 | 0.21 | -0.40 | 0.00 | -0.02 |
| 190 | 0.00 | -0.10 | 0.10 | -0.05 | 0.54 | 1.25 | 0.06 | -0.40 | 0.00 | -0.02 |
| 192 | 0.00 | -0.10 | 0.10 | -0.05 | 0.20 | 1.20 | 0.21 | -0.40 | 0.00 | 0.00 |
| 194 | 0.00 | -0.05 | 0.10 | -0.02 | 0.18 | 1.68 | 0.73 | -0.20 | 0.00 | -0.02 |
| 196 | 0.00 | -0.05 | 0.10 | 0.00 | 0.19 | 1.93 | 1.07 | -0.40 | 0.00 | 0.00 |
| $Z = 124$ | | | | | | | | | | |
| 170 | 0.00 | -0.20 | 0.02 | 0.02 | 0.04 | 2.10 | 0.93 | -0.50 | 0.06 | 0.05 |
| 172 | 0.00 | -0.20 | 0.06 | 0.02 | 0.58 | 9.22 | 0.94 | 0.40 | 0.00 | 0.05 |
| 174 | 0.00 | -0.20 | 0.06 | 0.02 | 0.77 | 10.31 | 1.06 | 0.40 | 0.00 | 0.05 |
| 176 | 0.00 | -0.20 | 0.08 | 0.00 | 0.75 | 10.21 | 0.56 | 0.40 | 0.02 | 0.02 |
| 178 | 0.00 | -0.25 | 0.08 | 0.00 | 0.19 | 9.13 | 0.58 | 0.40 | 0.03 | 0.02 |
| 180 | 0.00 | -0.15 | 0.08 | -0.02 | 0.10 | 8.51 | 0.70 | 0.40 | 0.00 | 0.02 |
| 182 | 0.00 | -0.15 | 0.10 | -0.05 | 0.87 | 8.78 | 0.89 | 0.40 | 0.00 | 0.02 |
| 184 | 0.00 | -0.15 | 0.10 | -0.02 | 1.67 | 2.48 | 2.24 | -0.40 | 0.00 | -0.05 |
| 186 | 0.00 | -0.15 | 0.10 | -0.05 | 0.78 | 1.89 | 1.25 | -0.40 | 0.00 | -0.05 |
| 188 | 0.00 | -0.10 | 0.10 | -0.05 | 0.32 | 1.31 | 0.06 | -0.40 | 0.00 | -0.05 |
| 190 | 0.00 | -0.10 | 0.10 | -0.05 | 0.21 | 1.38 | 0.09 | -0.40 | 0.00 | -0.02 |
| 192 | 0.00 | -0.10 | 0.10 | -0.05 | 0.24 | 2.42 | 0.24 | -0.40 | 0.00 | 0.00 |
| 194 | 0.00 | -0.05 | 0.10 | -0.02 | 1.26 | 2.49 | 1.26 | -0.25 | 0.00 | -0.02 |
| 196 | 0.00 | -0.05 | 0.10 | 0.00 | 1.10 | 2.37 | 1.17 | -0.45 | 0.05 | 0.00 |
| $Z = 126$ | | | | | | | | | | |
| 170 | 0.00 | -0.15 | 0.02 | 0.02 | 0.07 | 2.16 | 0.67 | -0.50 | 0.06 | 0.05 |
| 172 | 0.00 | -0.20 | 0.06 | 0.02 | 0.29 | 3.01 | 2.36 | -0.50 | 0.06 | 0.07 |
| 174 | 0.00 | -0.20 | 0.06 | 0.00 | 0.52 | 9.49 | 0.89 | 0.40 | 0.00 | 0.05 |
| 176 | 0.00 | -0.20 | 0.08 | 0.00 | 0.69 | 10.01 | 0.47 | 0.40 | 0.00 | 0.02 |
| 178 | 0.00 | -0.20 | 0.08 | 0.20 | 0.14 | 2.43 | 4.15 | 0.05 | 0.00 | -0.02 |
| 180 | 0.00 | -0.15 | 0.08 | -0.02 | 0.13 | 3.43 | 4.41 | 0.05 | 0.00 | -0.02 |
| 182 | 0.00 | -0.15 | 0.10 | -0.05 | 0.62 | 4.18 | 3.65 | 0.05 | 0.00 | -0.02 |
| 184 | 0.00 | -0.15 | 0.10 | -0.05 | 1.39 | 2.21 | 1.68 | -0.40 | 0.00 | -0.07 |
| 186 | 0.00 | -0.15 | 0.10 | -0.05 | 0.67 | 1.62 | 0.76 | -0.40 | 0.00 | -0.05 |
| $Z = 128$ | | | | | | | | | | |
| 170 | 0.00 | -0.20 | 0.02 | 0.00 | 0.21 | 2.26 | 0.25 | -0.50 | 0.06 | 0.07 |
| 172 | 0.00 | -0.20 | 0.06 | 0.00 | 0.45 | 3.04 | 1.89 | -0.50 | 0.06 | 0.07 |
| 174 | 0.00 | -0.20 | 0.06 | 0.00 | 0.83 | 4.27 | 3.55 | -0.55 | 0.08 | 0.07 |
| 176 | 0.00 | -0.20 | 0.08 | 0.00 | 1.02 | 9.68 | 1.97 | 0.40 | 0.00 | 0.02 |
| 178 | 0.00 | -0.20 | 0.08 | -0.20 | 0.18 | 2.89 | 4.77 | 0.05 | 0.00 | 0.00 |
| 180 | 0.00 | -0.20 | 0.08 | -0.02 | 0.17 | 3.79 | 4.98 | 0.05 | 0.00 | 0.00 |
| 182 | 0.00 | -0.20 | 0.08 | -0.05 | 1.39 | 4.57 | 4.07 | 0.05 | 0.00 | 0.00 |
| 184 | 0.00 | -0.20 | 0.08 | -0.05 | 1.44 | 1.73 | 0.85 | -0.40 | 0.00 | -0.05 |
| 186 | 0.00 | -0.20 | 0.08 | -0.05 | 0.99 | 1.36 | 0.21 | -0.40 | 0.00 | -0.05 |
| $Z = 130$ | | | | | | | | | | |
| 172 | 0.00 | -0.20 | 0.06 | 0.00 | 0.38 | 2.84 | 0.88 | -0.55 | 0.08 | 0.07 |
| 174 | 0.00 | -0.20 | 0.06 | 0.00 | 0.77 | 3.45 | 2.36 | -0.55 | 0.10 | 0.07 |
| 176 | 0.00 | -0.20 | 0.08 | 0.00 | 0.60 | 4.74 | 3.24 | -0.55 | 0.10 | 0.07 |
| 178 | 0.00 | -0.20 | 0.08 | -0.20 | 0.15 | 3.66 | 2.78 | -0.90 | 0.22 | 0.12 |
| 180 | 0.00 | -0.20 | 0.08 | -0.02 | 0.51 | 4.87 | 2.31 | -0.90 | 0.22 | 0.12 |
| 182 | 0.00 | -0.20 | 0.08 | -0.05 | 0.39 | 4.44 | 1.32 | -0.90 | 0.22 | 0.12 |
| 184 | 0.00 | -0.20 | 0.08 | -0.05 | 0.67 | 1.01 | 0.26 | -0.40 | 0.00 | -0.05 |

TABLE V. (*Continued.*)

| N | D_{3h} minimum | | | Barrier | | Competing minimum | | | | |
|-----------|------------------|---------------|---------------|---------------|--------------|-------------------|--------|---------------|---------------|---------------|
| | Energy | α_{20} | α_{33} | α_{40} | $B_{D_{3h}}$ | B_{sep} | Energy | α_{20} | α_{33} | α_{40} |
| $Z = 132$ | | | | | | | | | | |
| 176 | 0.00 | -0.20 | 0.09 | 0.00 | 0.91 | 2.81 | 0.39 | -0.90 | 0.21 | 0.12 |
| $Z = 134$ | | | | | | | | | | |
| 176 | 0.00 | -0.20 | 0.09 | 0.00 | 1.57 | 4.82 | 1.65 | -0.90 | 0.21 | 0.12 |
| $Z = 136$ | | | | | | | | | | |
| 180 | 0.00 | -0.20 | 0.09 | 0.03 | 0.72 | 1.43 | 1.53 | -0.35 | 0.00 | 0.06 |
| 182 | 0.00 | -0.15 | 0.09 | 0.06 | 1.27 | 1.37 | 1.27 | -0.35 | 0.00 | 0.06 |
| $Z = 138$ | | | | | | | | | | |
| 182 | 0.00 | -0.15 | 0.09 | 0.06 | 1.43 | 1.09 | 1.31 | -0.35 | 0.00 | 0.06 |
| 184 | 0.00 | -0.15 | 0.09 | 0.06 | 1.57 | 1.54 | 1.20 | -0.35 | 0.00 | 0.06 |
| 186 | 0.00 | -0.15 | 0.09 | 0.06 | 1.88 | 1.03 | 1.88 | -0.40 | 0.00 | 0.09 |

Let us notice that in all the results presented in Tables IV and V, the D_{3h} -symmetry minima present the ground states, whereas the competing minima at about 1 to 5 MeV excitations may correspond to extreme oblate shapes. Again the barriers separating the twin minima are often negligibly small, significantly below 1 MeV. Returning to the discussion in Sec. IV we may suggest that the experimental manifestations of those structures via collective vibrations will have the form of relatively high lying 0-phonon and 1-phonon structures with the separate excitation energies (in contrast with the parity doublets).

- [1] Y. T. Oganessian, *J. Phys. G* **34**, R165 (2007).
- [2] A. Sobczewski and K. Pomorski, *Prog. Part. Nucl. Phys.* **58**, 292 (2007).
- [3] Y. T. Oganessian and V. Utyonkov, *Rep. Prog. Phys.* **78**, 036301 (2015).
- [4] S. Hofmann, S. Heinz, R. Mann, J. Maurer, G. Müntenberg, S. Antalic, W. Barth, H. G. Burkhard, L. Dahl, K. Eberhardt, R. Grzywacz, J. H. Hamilton, R. A. Henderson, J. M. Kenneally, B. Kindler, I. Kojouharov, R. Lang, B. Lommel, K. Miernik, D. Miller, K. J. Moody *et al.*, *Eur. Phys. J. A* **52**, 1 (2016).
- [5] S. Hofmann, in *EPJ Web of Conferences* (EDP Sciences, 2018), Vol. 182, p. 02054.
- [6] L. A. Malov, G. G. Adamian, N. V. Antonenko, and H. Lenske, *Phys. Rev. C* **104**, 064303 (2021).
- [7] J. Yang, J. Dudek, I. Dedes, A. Baran, D. Curien, A. Gaamouci, A. Gózdź, A. Pędrak, D. Rouvel, H. L. Wang, and J. Burkat, *Phys. Rev. C* **105**, 034348 (2022).
- [8] Focus issue to celebrate the 40-year anniversary of the 1975 Nobel Prize to Aage Niels Bohr, Ben Roy Mottelson, and Leo James Rainwater, *IoP Publishing | Royal Swedish Academy of Sciences* (IoP Publishing, Bristol, England, 2016), edited by J. Dudek, *Phys. Scr.* **91**, 023005 (2016).
- [9] Yu. Ts. Oganessian, V. K. Utyonkov, Y. V. Lobanov, F. Sh. Abdullin, A. N. Polyakov, I. V. Shirokovsky, Yu. S. Tsyganov, G. G. Gulbekian, S. L. Bogomolov, B. N. Gikal, A. N. Mezentsev, S. Iliev, V. G. Subbotin, A. M. Sukhov, G. V. Buklanov, K. Subotic, M. G. Itkis, K. J. Moody, J. F. Wild, N. J. Stoyer, M. A. Stoyer, and R. W. Lougheed, *Phys. Rev. Lett.* **83**, 3154 (1999).
- [10] Yu. Ts. Oganessian, V. K. Utyonkov, Yu. V. Lobanov, F. Sh. Abdullin, A. N. Polyakov, I. V. Shirokovsky, Yu. S. Tsyganov, G. G. Gulbekian, S. L. Bogomolov, A. N. Mezentsev, S. Iliev, V. G. Subbotin, A. M. Sukhov, A. A. Voinov, G. V. Buklanov, K. Subotic, V. I. Zagrebaev, and M. G. Itkis, J. B. Patin, K. J. Moody, J. F. Wild, M. A. Stoyer *et al.*, *Phys. Rev. C* **69**, 021601(R) (2004).
- [11] Yu. Ts. Oganessian, V. K. Utyonkov, Y. V. Lobanov, F. Sh. Abdullin, A. N. Polyakov, R. N. Sagaidak, I. V. Shirokovsky, Yu. S. Tsyganov, A. A. Voinov, G. G. Gulbekian, S. L. Bogomolov, B. N. Gikal, A. N. Mezentsev, S. Iliev, V. G. Subbotin, A. M. Sukhov, K. Subotic, V. I. Zagrebaev, G. K. Vostokin, M. G. Itkis, K. J. Moody, J. B. Patin *et al.*, *Phys. Rev. C* **74**, 044602 (2006).
- [12] Yu. Ts. Oganessian, F. S. Abdullin, P. D. Bailey, D. E. Benker, M. E. Bennett, S. N. Dmitriev, J. G. Ezold, J. H. Hamilton, R. A. Henderson, M. G. Itkis, Yu. V. Lobanov, A. N. Mezentsev, K. J. Moody, S. L. Nelson, A. N. Polyakov, C. E. Porter, A. V. Ramayya, F. D. Riley, J. B. Roberto, M. A. Ryabinin *et al.*, *Phys. Rev. Lett.* **104**, 142502 (2010).
- [13] Information extracted from the NuDat database 2022, National Nuclear Data Center (NNDC), <https://www.nndc.bnl.gov/nudat/>.
- [14] Y. T. Oganessian, V. K. Utyonkov, Y. V. Lobanov, F. Sh. Abdullin, A. N. Polyakov, R. N. Sagaidak, I. V. Shirokovsky, Yu. S. Tsyganov, A. A. Voinov, A. N. Mezentsev, V. G. Subbotin, A. M. Sukhov, K. Subotic, V. I. Zagrebaev, S. N. Dmitriev, R. A. Henderson, K. J. Moody, J. M. Kenneally, J. H. Landrum, D. A. Shaughnessy, M. A. Stoyer, N. J. Stoyer *et al.*, *Phys. Rev. C* **79**, 024603 (2009).
- [15] V. I. Zagrebaev and W. Greiner, *Phys. Rev. C* **78**, 034610 (2008).
- [16] V. I. Zagrebaev and W. Greiner, *Phys. Rev. C* **83**, 044618 (2011).

- [17] G. G. Adamian and N. V. Antonenko, *Eur. Phys. J. A* **58**, 111 (2022).
- [18] A. Sobiczewski, F. Gareev, and B. Kalinkin, *Phys. Lett.* **22**, 500 (1966).
- [19] J. Dudek, *Acta Phys. Polon. B (Poland)* **9**, 919 (1978).
- [20] K. Rutz, M. Bender, T. Bürvenich, T. Schilling, P. G. Reinhard, J. A. Maruhn, and W. Greiner, *Phys. Rev. C* **56**, 238 (1997).
- [21] S. Patra, W. Greiner, and R. K. Gupta, *J. Phys. G* **26**, L65 (2000).
- [22] D. Vautherin and D. Brink, *Phys. Rev. C* **5**, 626 (1972).
- [23] S. Cwiok, W. Nazarewicz, and P. H. Heenen, *Phys. Rev. Lett.* **83**, 1108 (1999).
- [24] R. K. Gupta, S. Patra, and W. Greiner, *Mod. Phys. Lett. A* **12**, 1727 (1997).
- [25] A. Gaamouci, I. Dedes, J. Dudek, A. Baran, N. Benhamouda, D. Curien, H. L. Wang, and J. Yang, *Phys. Rev. C* **103**, 054311 (2021).
- [26] V. M. Strutinsky, *Nucl. Phys. A* **95**, 420 (1967); **122**, 1 (1968).
- [27] M. Brack, J. Damgaard, A. S. Jensen, H. C. Pauli, V. M. Strutinsky, and C. Y. Wong, *Rev. Mod. Phys.* **44**, 320 (1972).
- [28] The *Universal Woods-Saxon Hamiltonian* and associated, so-called ‘universal parametrization’ has been developed in a series of articles: J. Dudek and T. Werner, *J. Phys. G: Nucl. Phys.* **4**, 1543 (1978); J. Dudek, A. Majhofer, J. Skalski, T. Werner, S. Cwiok, and W. Nazarewicz, *ibid.* **5**, 1359 (1979); J. Dudek, W. Nazarewicz, and T. Werner, *Nucl. Phys. A* **341**, 253 (1980); J. Dudek, Z. Szymański, and T. Werner, *Phys. Rev. C* **23**, 920 (1981); and has been summarized in S. Cwiok, J. Dudek, W. Nazarewicz, J. Skalski, and T. Werner, *Comput. Phys. Commun.* **46**, 379 (1987). This approach is being used without modifications by many authors also today.
- [29] To illustrate the use-frequency of the “universal” Woods-Saxon phenomenological mean-field Hamiltonian we quote below the articles which appeared only in one year (2013) and only in one journal: J. Rissanen, R. M. Clark, K. E. Gregorich, J. M. Gates, C. M. Campbell, H. L. Crawford *et al.*, *Phys. Rev. C* **88**, 044313 (2013); W. Brodziński and J. Skalski, *ibid.* **88**, 044307 (2013); S. Lalkovski, A. M. Bruce, A. M. Denis Bacelar, M. Górska, S. Pietri, Z. Podolyak *et al.*, *ibid.* **88**, 024302 (2013); H. L. Liu and F. R. Xu, *ibid.* **87**, 067304 (2013); D. S. Delion and R. J. Liotta, *ibid.* **87**, 041302(R) (2013); D. S. Delion, R. J. Liotta, and R. Wyss, *ibid.* **87**, 034328 (2013); D. S. Delion and J. Suhonen, *ibid.* **87**, 024309 (2013); D. Deleanu, D. L. Balabanski, T. Venkova, D. Bucurescu, N. Mărginean, E. Ganioglu *et al.*, *ibid.* **87**, 014329 (2013).
- [30] H. J. Krappe, J. R. Nix, and A. J. Sierk, *Phys. Rev. C* **20**, 992 (1979).
- [31] P. Möller, J. Nix, W. Myers, and W. Swiatecki, *At. Data Nucl. Data Tables* **59**, 185 (1995).
- [32] J. Yang, J. Dudek, I. Dedes, A. Baran, D. Curien, A. Gaamouci, A. Gózdź, A. Pe, drak, D. Rouvel, and H. L. Wang, *Phys. Rev. C* **106**, 054314 (2022).
- [33] D. Rouvel and J. Dudek, *Phys. Rev. C* **99**, 041303(R) (2019).
- [34] S. C. Pancholi, *Pear-Shaped Nuclei* (World Scientific, Singapore, 2020).
- [35] D. A. Varshalovich, A. N. Moskalev, and V. K. Khersonskii, *Quantum Theory of Angular Momentum* (World Scientific, Singapore, 1988).
- [36] A. Bohr and B. R. Mottelson, *Nuclear Structure* (W. A. Benjamin, Reading, 1975), Vol. 2.
- [37] W. Nazarewicz, P. Olanders, I. Ragnarsson, J. Dudek, and G. A. Leander, *Phys. Rev. Lett.* **52**, 1272 (1984).